

High-Gain Microfluidic Amplifiers: The Bridge between Microfluidic Controllers and Fluidic Soft Actuators

Elizabeth Gallardo Hevia,* Connor M. McCann, Michael Bell, Nak-seung Patrick Hyun, Carmel Majidi, Katia Bertoldi, and Robert J. Wood

Soft fluidic robots are typically controlled using manifolds containing large and rigid electromechanical valves. These bulky controllers limit scalability and hinder motion, in particular for untethered soft robots. There has been recent interest in using fluidic controllers analogous to electrical logic gates and microcontrollers to replace rigid valve systems. However, these microfluidic networks typically operate with small volumes, low flow rates, and low pressures relative to what is needed to power fluidic soft actuators. This article presents the design, fabrication, and analysis of a soft, fluidic amplifier as the “missing link” between microfluidic analogies of microcontrollers and the high fluidic power loads representative of soft actuators. The article demonstrates amplification gains of pressure signals up to a factor of four. The amplifier is a step toward fully autonomous soft robots by allowing designers to develop control strategies from soft materials with minimal additional rigid components or tethering.

1. Introduction

The field of soft robotics has emerged to explore the potential for soft materials to transform traditional, predominantly rigid robots into more robust, safe, and compliant forms. The properties of soft robots—compliance, back-drivability, inherent safety—have made them appropriate for handling fragile objects,^[1] as corobotic assistive devices,^[2] and in navigating irregular terrain and confined spaces.^[3,4] The last several decades have been marked by notable soft robot demonstrations in academic settings, including grippers for

gathering delicate deep-sea organisms,^[5] assistive devices for muscle injury prone factory workers,^[6,7] and to augment human experiences through haptic communication.^[8,9] Although we can easily imagine soft robots independently operating in/on the human body or responding to stimuli while in a search and rescue site, soft robots have been primarily actuated fluidically and tethered for fluidic power and control,^[10] thereby limiting autonomy for these use cases or requiring (often rigid) hardware for controlling fluidic pressure and flow.^[11]

There have been efforts to move some of this fluidic power and control on-board, thereby decreasing the reliance on bulky and rigid external hardware.^[12] Of the current approaches adopted, following in the footsteps of Wehner et al.^[11] and Bartlett et al.,^[13] we propose the following


steps for using microfluidic circuits for low-level motion control. Microfluidics is a mature field which contains decades' worth of literature related to the design and operation of logic circuits to control small-volume flow within soft substrates.^[14,15] In our last work, we have explored microfluidic circuits that produce functionalities akin to electronic microcontrollers and adapted them to realize circuits made solely of soft structures.^[16] However, for microfluidic circuits to be an appropriate option for soft robot control, such as in typical electronic control systems, control signals to electromechanical actuators (e.g., from microcontrollers) require amplification to enable the device to perform useful work.

In this work, we develop a fluidic amplifier to convert low-magnitude flow and pressure inputs into ranges relevant for common soft fluidic actuators. The amplifier manipulates a channel carrying high-pressure and flow rates using a low pressure input. We demonstrate a fluidic soft amplifier producing a pressure gain of approximately four at 0.2 Hz.

The fluidic amplifier architectures and results presented here are a step toward embedded controllers for fully soft, untethered robots. We propose augmenting the capabilities of microfluidic-controlled soft robots by implementing a critical component—a fluidic amplifier. We describe design principles, manufacturing techniques, analysis of the valve, and, lastly, overall amplifier performance. We demonstrate the capabilities of this amplifier by comparing the actuation profiles of a system with and without the inclusion of the amplifier to drive a common fluidic actuator.

E. Gallardo Hevia, C. M. McCann, M. Bell, N. Hyun, K. Bertoldi, R. J. Wood
School of Engineering and Applied Sciences
Harvard University
Science and Engineering Complex
150 Western Ave, Boston, MA 02134, USA
E-mail: gallardo@g.harvard.edu

C. Majidi
Mechanical Engineering Department
Carnegie Mellon University
5000 Forbes Avenue, Pittsburgh, PA 15213, USA

 The ORCID identification number(s) for the author(s) of this article can be found under <https://doi.org/10.1002/aisy.202200122>.

© 2022 The Authors. Advanced Intelligent Systems published by Wiley-VCH GmbH. This is an open access article under the terms of the Creative Commons Attribution License, which permits use, distribution and reproduction in any medium, provided the original work is properly cited.

DOI: 10.1002/aisy.202200122

2. Design Overview

2.1. Concepts for High-Gain Valves

We have identified four frameworks to categorize the general architectures of soft, fluidic amplifiers. In this section, we explain the operating principle for each framework, describe efforts that have been explored previously, and suggest applications where they may be most suitable. We grouped the frameworks based on amplification modality—i.e., flow or pressure gain (see Figure 1). The frameworks are categorized as follows

2.1.1. Microfluidic Channel Scaling

One simple method to increase volumetric flow rate and reduce pressure drops across small channels is to physically enlarge the dimensions of a microfluidic controller. The desired scaling should be based on the maximum acceptable pressure drop due to the impedance of a channel. The channel impedance and pressure drop can be calculated using the Hagen–Poiseuille equation^[17]

$$\Delta P = \frac{8LQ\mu}{\pi R^4} \quad (1)$$

which is a close approximation (for laminar flow conditions) of the pressure drop (ΔP) across a channel of known dimensions (channel length, L , and radius, R) and viscosity (μ) given fluid flow rate (Q). An alternate approach to enlarging channels is to combine several identical microfluidic networks in parallel to achieve the equivalent desired large flow rates.

2.1.2. Fluid Entrainment

Another concept for flow amplification is fluid entrainment. This phenomenon can be thought of as a form of fluidic advantage where a low pressure, low flow control input is capable of manipulating a low pressure, high-flow signal input resulting in a high signal at one of the two outputs. Bistable devices that employ fluid entrainment leverage the Coandă effect to cause a high-flow fluid stream to flow through one of the two output legs at a time.^[18]

2.1.3. Structural Instabilities

Mechanical instabilities offer an alternative method for control. A notable example is the pressure-amplifying bistable valve demonstrated by Rothmund et al. which leveraged a snapping mechanism to amplify the pressure and flow from an input signal to pinch a high channel carrying a fluid of high pressure and flow. Although this device was several centimeters in scale (i.e., not leveraging microfluidic valves or soft lithography-based fabrication techniques), by combining multiple valves together the authors demonstrated a functionally complete set of logic gates.

2.1.4. Mechanical Advantage

The final amplifier class leverages mechanical advantage to manipulate a high-pressure flow with a low pressure input signal. Mechanical advantage is the ratio of the force produced by a device relative to the force applied to it; the amplification is accompanied with a trade-off of some other parameter such that,

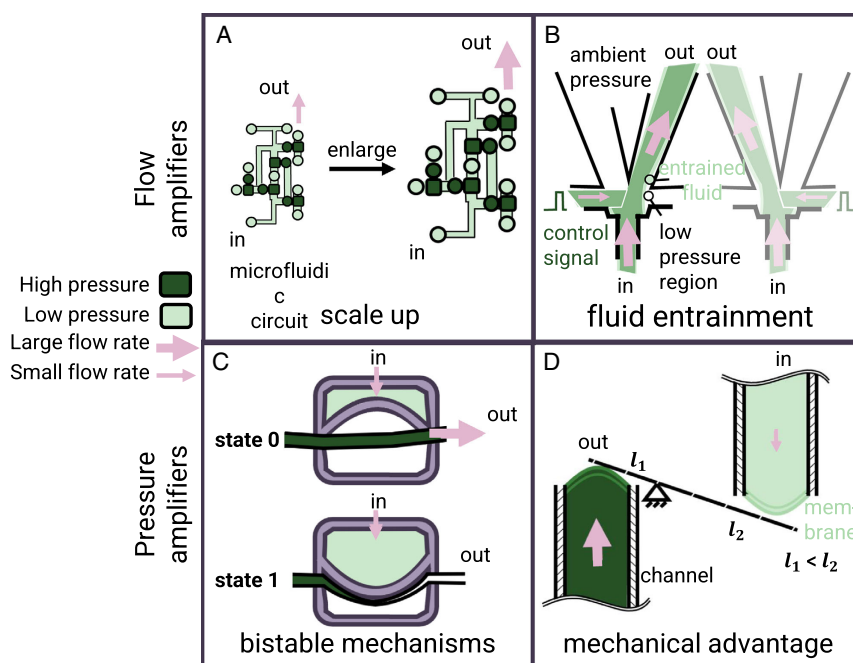


Figure 1. Concept images of four potential frameworks for a high-gain valve design: A) scaling up channel dimensions; B) fluid entrainment using a low-flow control input; C) bistable mechanisms that can switch between two states with a low pressure input; and D) mechanical advantage. Input and output flow is depicted in green with the flow direction indicated by pink arrows where the arrow size indicates the magnitude of the associated flow rate.

ideally, the work in is equal to the work out. In our designs, a low pressure input is used to generate a large force by acting over a large area. This force is coupled to a relatively smaller area indenter which closes off a channel carrying the working fluid for a fluidic actuator. The use of mechanical advantage to produce gain has been seen before.^[19–21]

While each of these techniques has merit for certain use cases, the mechanical advantage framework is the most appropriate for continuous modulation of pressure and flow in high impedance loads, and thus we focus primarily on this concept for amplifier development. Furthermore, this concept allows us to leverage a wealth of microfluidic design and fabrication techniques for both the controller and the amplifier independently of each other.

3. Performance Metrics

We chose two performance-related metrics to guide the final design of the amplifier: gain and response time (analogous to the gain-bandwidth product in electrical amplifiers). In this section, we will define these metrics and use them to guide design decisions to optimize the amplifier's performance. The primary purpose of an amplifier is to increase the power of an input signal and to impedance match to a load impedance to maximize efficiency. Power in a fluidic system is the product of pressure and volumetric flow rate. Therefore, we will discuss two types of amplification gain modes: flow gain and pressure gain.

Flow gain has the potential to be useful for low impedance fluidic actuators that require low pressures but large continuous or intermediate flow rates. Generally speaking, low impedance is the result of an actuator with relatively large internal volume or low modulus components. The fluid entrainment work discussed earlier ceased to function properly when attached to loads of impedances greater than $0.050 \text{ kg mm}^{-4} \text{ s}^{-1}$.^[18] Given the absence of standard impedance magnitudes to define the bounds of a "low-impedance" actuator, we use this value as a maximum limit.

Pressure gain can be used for medium to high impedance actuators that require high pressures to move the necessary volumes of fluid to deform the actuators. Given the dominance of pressure-controlled actuators in the soft robotics literature, the focus of this article is primarily on high-gain valves for pressure-mode actuators. We define pressure gain to be the ratio of the output to input pressures (We also consider power gain where power is the product of pressure and volumetric flow rate. However, for pressure-mode actuators, flow rates will tend to zero once the commanded pressure is achieved; thus, while peak power and peak power gain may be a useful metric, this will vary as a function of actuator state.).

To define the target ranges for output and input pressures, we surveyed soft actuators and microfluidic circuits. The ranges of values noted here and in the remainder of this section will be used to define the ranges of our targets for the metrics mentioned; despite quoted data for these measurements being sparse in the literature, we found that a common command input for soft actuators is 103.4 kPa ^[22–28] while microfluidic output signals vary from 3.4 to 34.5 kPa due to the large resistances of the narrow channels which cause a large pressure drop limiting the output pressure at flow rates relevant to typical soft fluidic

actuators.^[29] Therefore, a gain range that guarantees that all microfluidic output signal magnitudes can be amplified to drive the largest soft robotic loads is $3\text{--}30$.

Although we are primarily interested in pressure control, we must also specify input flow rates to the amplifier, and therefore, the input impedance. Similarly, in order to maximize power in the load, we must consider the output flow rate and output impedance. Input flow rates will affect the response time of the amplifier while the output flow rate requirements will depend on the load being driven. The flow rates relevant to soft robotics can range anywhere between one and tens of liters per minute.^[22] Actuating a component of much larger physical scale (fluidic actuators described in previous research have internal volumes ranging from hundreds of microliters to tens of milliliters) compared to the small channels that make up microfluidic devices makes the task extremely slow because of the inherently low flow rates ($0.01\text{--}10 \text{ mL min}^{-1}$) typical of microfluidic devices.^[30,31] A fluidic amplifier with a large input impedance (at least as large as the output impedance of a typical microfluidic control stage) can resolve the incompatibility between the two stages similar to how a MOSFET input in a class-A electrical amplifier ensures sufficiently high input impedance so as not to distort the input signal.

Ideally, the total response time for the amplifier should be less than the inverse of the microfluidic circuit's clock frequency. In other words, the amplifier bandwidth should have a minimum bound no lower than that of the fundamental frequency of the microfluidic circuit's clock so that the output of the overall system (i.e., microfluidic circuit and amplifier combined) is not attenuated. Similar to considerations for the input capacitance of transistors, the volume of the proposed high-gain valve's input cavity should be minimized to ensure that the input impedance is maximal at high frequencies.

A related consideration is the response time of the soft actuators; similar to the previously stated requirement, the amplifier should operate at speeds faster than those of the actuator so that the amplifier is not a bottleneck for the overall system response time. Soft fluidic actuators are typically actuated at frequencies below 1 Hz .^[12] Therefore, we are targeting a minimum amplifier bandwidth of 0.25 Hz .

4. Soft, Fluidic Power Amplifier

4.1. Amplifier Design Considerations

In the following section, we describe the design for the fluidic amplifier, explore its design space, and select a final design for further characterization. The amplifier can be described using a p-channel metal oxide semiconductor (pMOS) transistor analogy where we identify a gate, source, and drain (see Figure 2B). Similar to a pMOS transistor where a positive voltage at the gate would stop conduction through the source–drain, a positive pressure at the gate blocks flow through the source–drain of the fluidic amplifier while a null pressure at the gate causes it to conduct (see Figure 2C).

In our design, the indenter amplifies a signal by leveraging mechanical advantage. A low-pressure signal introduced at the gate interacts with a large gate input surface area

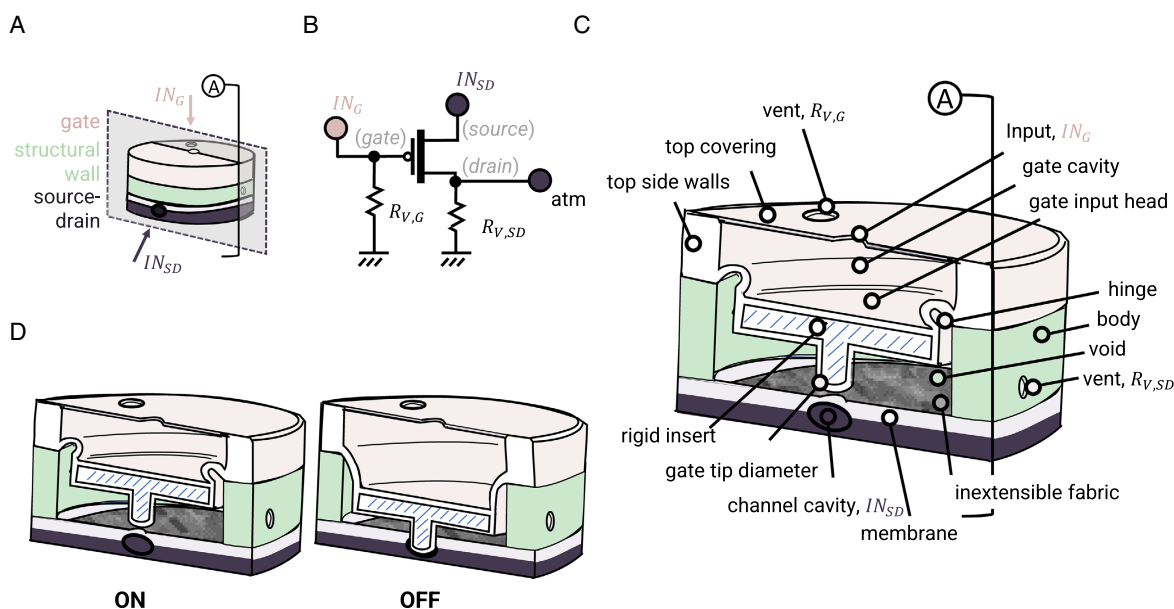


Figure 2. Details of the soft fluidic power amplifier. A) Illustration of the fluidic power amplifier with a comparison to pMOS terminology used to label the various components of the amplifier. B) Class-A electrical equivalent of the fluidic amplifier with inputs, outputs, and resistors labeled. C) A low power control signal input is introduced at the gate to produce an inverted and amplified output. The output is active, or “On,” when the input signal is low, allowing fluid to flow through the source–drain. When the control signal is high, the indenter moves into the channel, consequently blocking off flow through the source–drain. D) Schematic showing the components of the high-gain valve. The valve is made up of a retaining wall which holds the gate and source–drain components together, a channel which conducts flow from a source to a load, an indenter made up of a rigid insert covered in elastomer that translates up and down (depending on the gate pressure) to pinch off the source–drain channel, and a hinge which holds the indenter in place and isolates the gate input cavity.

(see Figure 2D) which produces a downward force at the indenter tip much larger than the force acting upward resisting the downward motion of the indenter tip. Although a higher pressure is present in the source–drain than the gate, the high pressure is only able to act over the smaller surface area of the indenter tip. Thus, the indenter is able to control a high-pressure and flow output using a low-pressure input.

In addition to the analogous gate and source–drain found in pMOS transistors, the fluidic amplifier similarly contains leaky resistors. The configuration of these components is inspired by a class-A amplifier architecture (see Figure 2B). In this setup, a resistor is placed both at the gate and source–drain. The output of the amplifier is an inverted and amplified replica of the command signal.

In the following sections, we describe the tests and analysis conducted to explore the design space of the gate and source–drain separately, and then combine these components to complete the amplifier.

4.1.1. Gate Design

At the gate, a radially symmetric indenter is able to translate vertically, guided by a thin flexible hinge. A control pressure is applied to the gate, and this pressure acts on the top face of the indenter. The extension of the indenter into the source–drain (or “power”) channel is determined by a force balance between the force acting on the gate input from the control

pressure and the resistive forces due to the membrane stiffness at the interface with the power channel, the pressure inside the power channel, and the indenter hinge stiffness. The entire body making up the gate subcomponent of the amplifier is fabricated via a single-step injection-molding process of silicone rubber, which enabled the formation of the thin curved membrane seamlessly connected to the rest of the gate (i.e., mechanical ground). This flexure both aligns the indenter upright vertically and separates, fluidically, the gate cavity from the intermediate (void) space in the body of the device. Because the indenter hinge has an impedance proportional to its stiffness, we sought to maximize the compliance through flexure geometry and material choice. True Skin 30 (CHT-Silicones, VA, USA) was chosen as the material to make up the gate due to its low stiffness (i.e., 30 A shore hardness). Structurally, the indenter is a 3D-revolved “T”; an isometric cross-sectional view is labeled in Figure 2D. A rigid insert made of a carbon fiber-filled nylon (Onyx, Markforged, MA, USA) was used as the core of the moving piece in the gate and is responsible for ensuring efficient force transfer from the gate input head to the tip—any undesired compliance can be considered similar to a parasitic capacitance.

We used finite element analysis (FEA) to explore the design space for the gate (details regarding the FE model are provided in Figure S2, Supporting Information). The design space includes variable parameters such as the indenter and hinge material, indenter tip geometry, and hinge eccentricity and thickness. We are interested in the parameters that maximize gain,

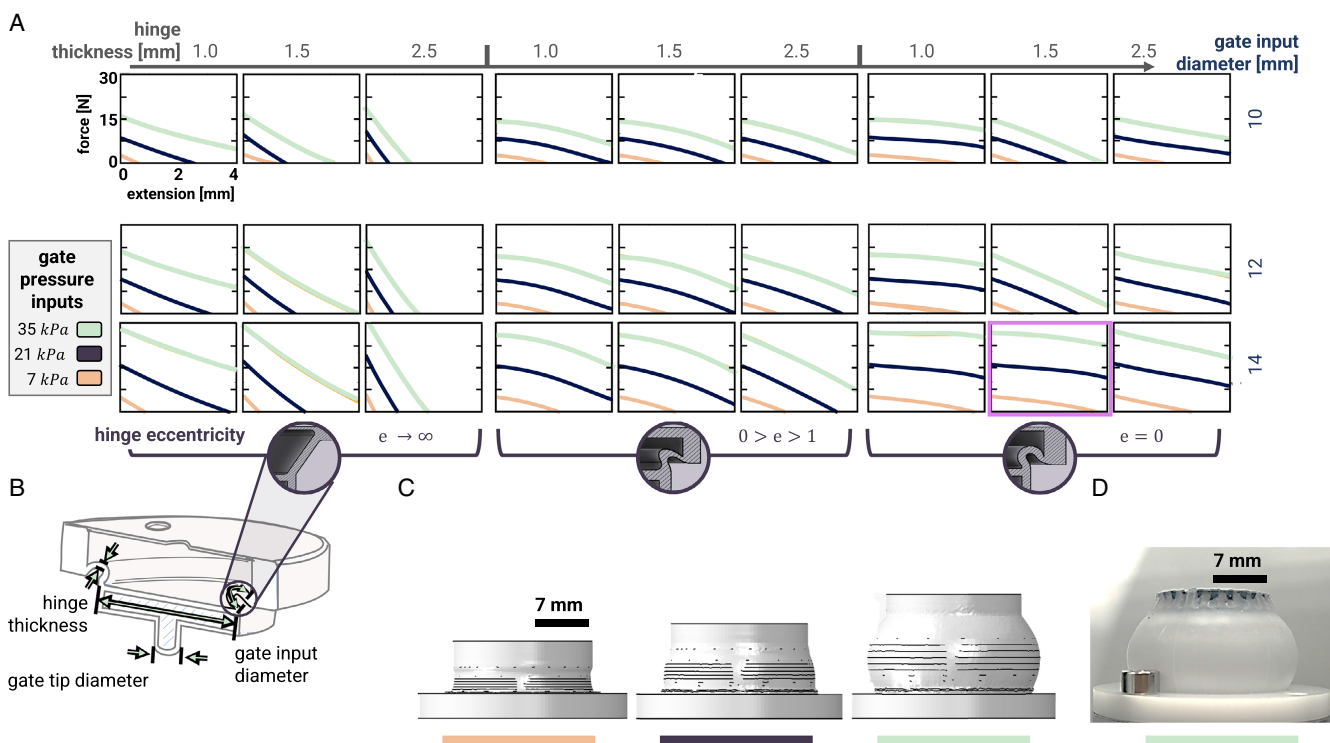


Figure 3. Gate design space exploration using FEA. FEA was used to study the various effects that key parameters of the gate design play on the FD curves associated with the extension of the gate tip at various pressure inputs. A) Results of the FEA study are grouped by three clusters depending on the hinge eccentricity of the design (indicated along the bottom row of (A)). Designs in each cluster display increasing hinge thicknesses along the horizontal axis and increasing gate input diameter along a downward vertical axis. The selected design is highlighted in dark pink. B) Key parameters are labeled: hinge thickness, gate input diameter, and hinge eccentricity. C) The simulated FEA model includes hinge thickness, gate input diameter, and supports various pressure inputs. FEA screenshots are provided of the gate pressurized at 7, 21, and 25 kPa as indicated by the color bars underneath. D) Image of the gate pressurized at 35 kPa.

i.e., parameters that produce the largest forces and maintain the force output throughout the gate's extension. This criterion can be applied to the force–displacement (FD) curves in **Figure 3**—the designs that will produce the largest gains are those with the largest maximum force value and shallowest slopes.

We first experimentally validated the FE results using a mechanical testing machine (Instron 5567, Instron, MA, USA—see Figure S3, Supporting Information, for details regarding the experimental procedure used). We then performed a parameter sweep using the FE software Abaqus (SIMULIA, RI, USA). The full study compared results for varying gate input diameter, hinge thickness, and hinge eccentricity for input pressures ranging from 7 to 35 kPa. The results of the simulations are shown in **Figure 3A** and the parameters under study are highlighted in **Figure 3B** for reference. Screenshots of the simulated gate model are provided in **Figure 3C** and an image of the fabricated gate used in a study is shown in **Figure 3D**.

In the resultant FD plots, zero extension is equivalent to an unactuated gate (i.e., the hinge is unstretched) while the maximum displacement corresponds to a gate that is actuated and, therefore, the gate tip has moved downward a maximum distance. A few remarks can be made about the results. First, the stretching of the hinge produces a resistive force that opposes the force from the input pressure. We note that an insignificant

increase in maximum force output up to 10% occurs as hinge thickness increases from 1.0 to 2.5 mm for hinge eccentricities less than 1; maximum force outputs increase up to 50% for linear hinges.

Second, large disparities in maximum forces are seen across the designs containing the same hinge thickness and hinge eccentricity but different gate input diameters due to the gate-area-dependent force of the indenter. For example, we see an increase up to 100% between the maximum forces as gate input diameter increases from 10 to 14 mm (as expected given the roughly doubling of the area).

Lastly, we compare the effect of hinge eccentricity. Eccentricity, e , is a measure of the similarity of a conic section to a circular shape. We define the eccentricity of the various hinge designs by treating them as portions of conic shapes. To define eccentricity, we use the ratio between major and minor axes of the hinges which we have labeled in further detail in **Figure S4**, Supporting Information.

We note that a flexure with eccentricity approaching infinity (i.e., a straight line) acts like a spring being stretched axially with a linear FD relationship. The resistive force of the hinge is initiated the moment the gate receives an input pressure and can be observed by a dramatic drop in slope of the FD curves. However, this is not observed for hinges containing

eccentricities of 0–1 because of their “deadzone” (defined in Figure S4, Supporting Information). The deadzone allows the gate to move downward without imparting resistive forces from the hinge. This translates to a minimal loss in force in the FD curves throughout the range of extensions shown.

Note, in the demonstrated designs, the thickness distribution along the elliptical hinge is not uniform throughout (see Figure S4, Supporting Information). However, as stated previously, thickness is less influential than the deadzone in the ranges of interest. Eccentricity is used as a proxy for deadzone which we conclude is the main contributor to a shallow slope. We use eccentricity because it produces the same trends as the deadzone; however, to conclude the effect of eccentricity, we would need to further investigate hinges with equal deadzone lengths.

A gate that can provide the highest force to the source–drain channel will produce the largest gain. In addition to maximizing gain, we aim to adopt a gate design that maintains a large force throughout its extension. Based on the above analysis, gate input diameter plays a primary role in the maximum force attainable while the deadzone of a hinge is responsible for maintaining the high output forces throughout the range of motion. For our final hinge design, we chose a hinge thickness of 1.5 mm, a gate input diameter of 14 mm, and an eccentricity of zero.

4.1.2. Source–Drain Design

The source–drain portion of the valve connects a high-pressure supply to a load. In this device, the source–drain consists of a channel with circular cross section embedded in an elastomeric matrix. When pressurized, fluid is able to pass through the channel at high-flow rates due to its relatively large diameter. When a control input signal is applied to the gate, the indenter moves down into the source–drain channel to block off flow. Although the pressure at the input of the gate is lower than the pressure in the channel, the force at the gate tip pushing down is larger than the force resisting the downward movement; the ratio between the surface area of the gate input to the gate tip is responsible for the observed mechanical advantage.

The experimental setup is shown in Figure 4A in which we used a mechanical testing machine (Instron) with a 3D printed gate core to push down on the source–drain design under investigation. We zeroed the Instron at the extensions at which the flow rate remained below 0.2 mL min^{-1} . The indenter was then placed above the source–drain without contact and moved down at a rate of 0.25 mm s^{-1} until it reached the closure criteria. The corresponding flow rate was measured throughout this period. Force measurements were collected for pressure inputs

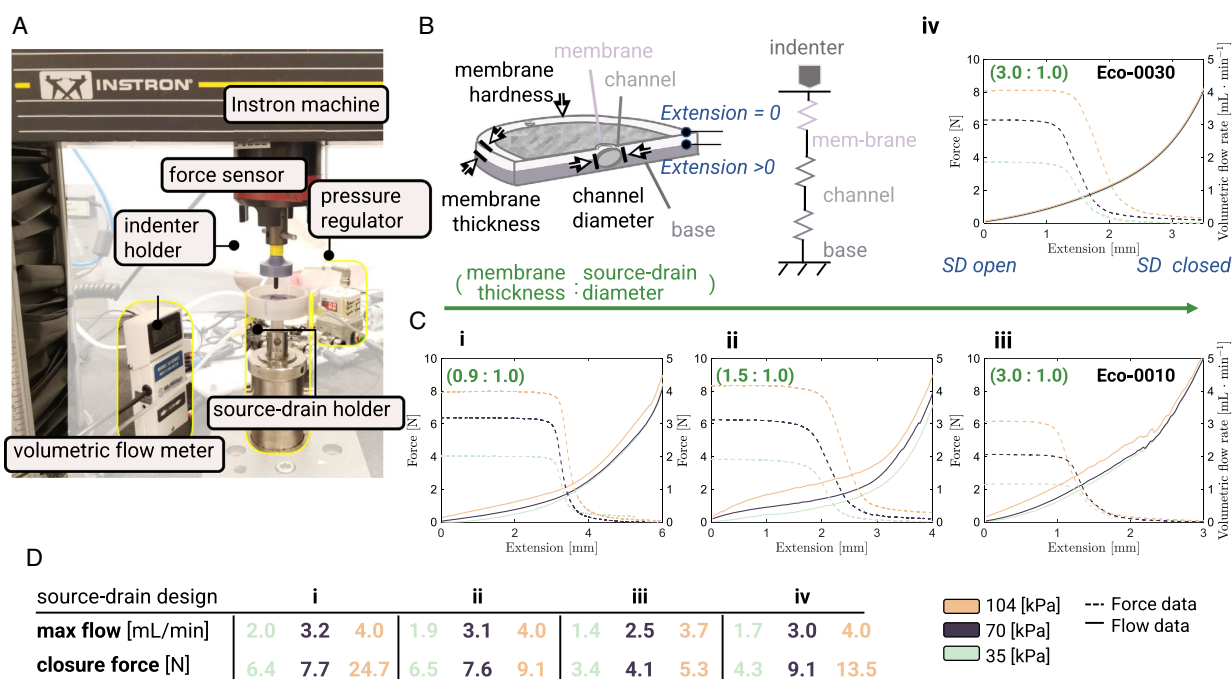


Figure 4. Source–drain design space analysis. A) The hardware components used for the tests are labeled. A mechanical testing machine was used to measure force and displacement; a pressure regulator provided precise pressure inputs to the source–drain; a volumetric flow meter was placed in series with the output of the source–drain venting to atmosphere; and custom rigs compatible with the mechanical testing machine were 3D printed and used to hold and align the indenter and source–drain. B) Key parameters of the source–drain under study that influence the amount of force required to deform the membrane are labeled. A lumped-parameter analytical model represents the various resistive forces that contribute to the overall forces required to close the source–drain plotted in (C). C) Experimentally derived FD curves show the effects that the ratio of membrane thickness to source–drain channel diameter has on the deformability of the membrane (i–iii) as well as membrane hardness (iv). Solid and dotted lines indicate empirically collected force and volumetric flow rate data, respectively. The membrane hardness, channel diameter, and membrane thicknesses used for each design are: i) 00–10, 2.5 mm, 2.25 mm; ii) 00–10, 1 mm, 1.5 mm; iii) 00–10, 1 mm, 3 mm; and iv) 00–30, 1 mm, 3 mm. The extension of the tip at 0 mm results in an open source–drain (S–D) whereas a closed source–drain occurs for flows less than 0.2 mL min^{-1} . D) Table of the forces required to close the source–drain and the maximum flow rates produced for each source–drain design, labeled according to (C).

ranging from 35 to 103.5 kPa (see Figure S5, Supporting Information, for full details regarding these studies).

When considering an optimal design for the source–drain channel, the following parameters were chosen to investigate their effect on the input–output behavior: membrane material hardness, membrane thickness, and channel diameter on the force required to close the source–drain (see Figure 4B).

Four different designs were tested. The corresponding force and flow versus displacement profiles for each design are shown in Figure 4Ci–iv. Membrane hardness varied between 00–10 and 00–30 shore hardness; channel diameters varied between 1 and 2.5 mm; and membrane thicknesses varied between 1.5 and 3.0 mm. Each design was assigned a dimensionless ratio of membrane thickness to source–drain diameter, as shown in green in Figure 4C. The FD plots show the force required to turn off (i.e., close) the source–drain. We define closure to occur when the flow rate through the source–drain drops below a certain threshold. We chose that threshold to be 0.2 mL min^{-1} which corresponds to flows that are a fifth of the range of flows within common microfluidic circuits; we classify these flow rates as insufficient to actuate soft robots at relevant speeds. Flow rate profiles (dotted lines) and the force (solid lines) required to close the source–drain for a given input pressure (color-coded) are shown in Figure 4C. The extension shown corresponds to relative extensions. Synchronization between the flow rate and force data is indirect. Force data were collected simultaneously with extension data; however, flow data were collected along with time. Based on the sampling rate of the data acquisition system used and the extension rate of the Instron, we converted time to extension to facilitate the interpretation of the data. The plots are the averages of three samples, three trials each.

From Figure 4C, we can make a few conclusions. First, we observe two linear regions in the FD relationships. A change in slope is noted as the gate pushes past the channel void where it experiences resistance from the membrane and channel pressure and makes contact with the base. To reach closure, the gate tip must pass this elbow point. Second, the switch between open and closed occurs happens over the course of 1–2 s (due to the slow commanded speed to eliminate any dynamic effects). More than half of the time that the source–drain is being closed, it retains flow rates within 10% of its maximum flow rate. In the following plots in Figure 4C, we included the flow profile as it begins to switch from open to close and has omitted the (near constant) flow leading up to the switch. Third, closure forces and maximum flow rates are listed in Figure 4D. Generally, we observe that closure forces increase with an increase in pressure inputs as expected. The occasion where that trend is not observed is due to the difficulties associated with aligning the gate tip with the center of the source–drain channel which results in higher closing forces. Fourth, the larger the membrane thickness to SD diameter ratio, the less force is required to close the channels. In these cases, the membrane thickness dominates the effective stiffness of the system. Lastly, we conclude that membranes made from materials with 00–10 (Ciii) and 00–30 (CiV) shore hardness require similar forces to deform. Therefore, selecting between these two materials is inconsequential.

Based on this analysis we selected a final source–drain design for the amplifier. The aim of the amplifier is to maximize gain which can be achieved by choosing the design that requires the

least amount of force to deform. We chose the design described by a 3:1 ratio of membrane thickness to SD diameter which is made up of a membrane with a low material hardness (i.e., 00–10) and thickness (i.e., 1.5 mm). In addition, although a larger channel diameter allows larger flow rates, we deemed flow rates averaging 1.5 mL min^{-1} to be sufficient and therefore decided to maximize pressure gain instead.

We note that the compliance of the membrane is critical to maximize gain; however, high elongation of the membrane accompanies its soft nature. A common mode of failure of the source–drain is ballooning and subsequent bursting of the channel. To avoid failure of the source–drain, we constrained the top of the membrane with an inextensible fabric (Ripstop coated sailcloth, Dimension Polyant, CT, USA). The attachment of the fabric was reinforced by applying additional SmoothSil-945 along the edges of the source–drain component. Without the fabric, the channel would burst repeatedly at pressures above 35 kPa. For more details on the design and fabrication of the source–drain, see Figure S6, Supporting Information.

4.2. Venting Ports

Venting ports are necessary for the gate and load to return to their unactuated states. The size of a vent port plays a role in the performance of both metrics of interest—the amplifier's gain and response time. The vent presents a trade-off between the two metrics: a small time constant (i.e., quick response time) can be achieved at the cost of a lower gain (see Figure 5Ai,Bi). In the data presented here, the maximum attainable pressure, P_{out} , is directly related to gain as described by

$$P_{\text{gain}} = \frac{P_{\text{out}}}{P_{\text{in}}} \quad (2)$$

We tested the response time and maximum pressure outputs for a range of vent hole sizes at the gate and drain separately. Plastic dispensing tips (dispensing tips with Luer lock connection, McMaster Carr, IL, USA) were used as venting nozzles; the vent impedance values were calculated to range from 0.082 to $0.74 \text{ kg mm}^{-4} \text{ s}^{-1}$ (see Section S7, Supporting Information, for derivation of venting nozzle impedance values).

Time constants were obtained by applying a step pressure input of 20 kPa at the gate and 55 kPa at the source–drain for various vent impedances. Pressure and flow rate measurements were taken at the locations indicated in Figure 5Aiv, Biv, Av, and Bv. Time constants, τ , plotted in Figure 5Aii,Bii for each step response were obtained by fitting the volumetric flow rate data through the vent to Equation (3) which describes the flow rate through the vent resistors (see Section S12, Supporting Information). Equation (3) represents an estimated model using first-order low-pass dynamics based on the electrical circuit analogs of the experimental setup shown in Figure 5Aiv,Biv

$$Q(t) = Q_{\infty} + (Q_0 - Q_{\infty})e^{-t/\tau} \quad (3)$$

where $Q(t)$ is the volumetric flow rate, Q_0 is the initial flow rate before $t = 0$, and Q_{∞} is steady state flow rate. Section S7, Supporting Information, provides details on the experiments used to determine the time constants.

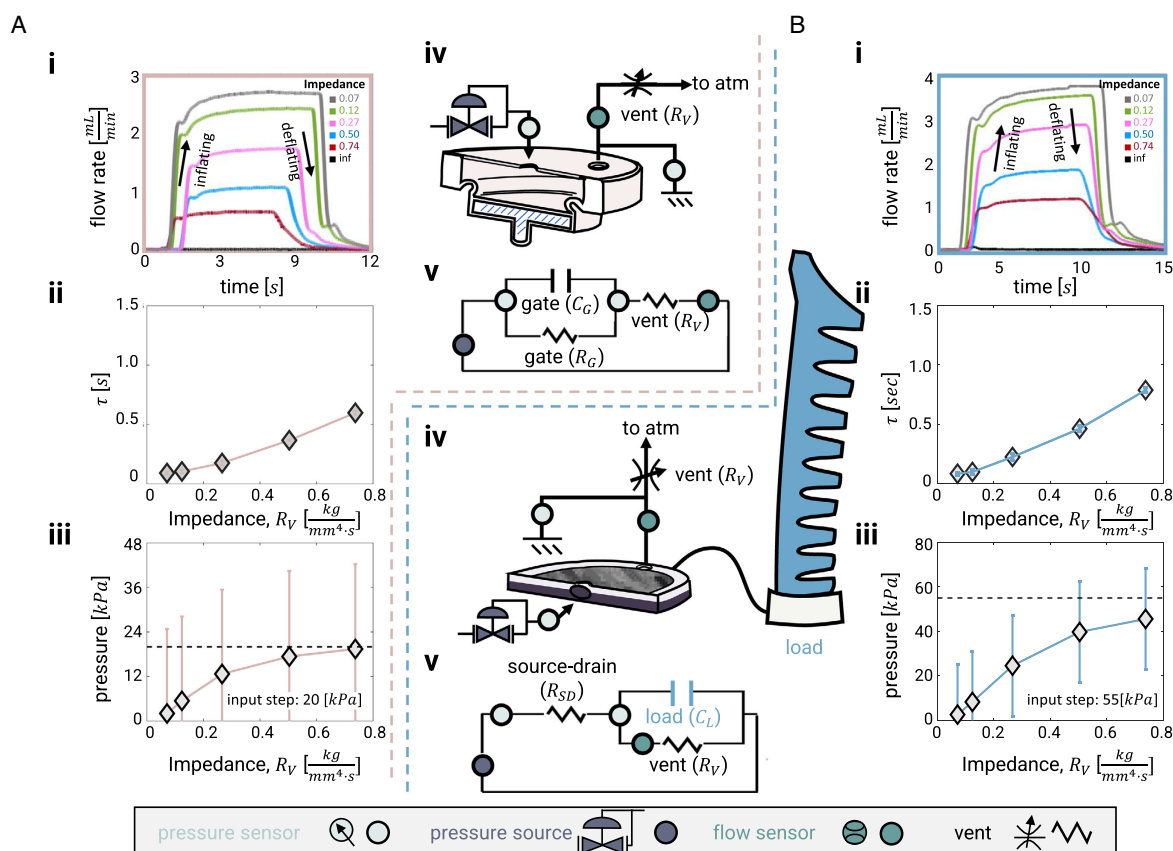


Figure 5. The effect of vent size on the system's response time and maximum pressures obtainable at the output. Studies are decoupled to focus on the behavior of the A) gate and B) source–drain independently. (i) Step-up and step-down flow responses to a step pressure input are displayed for various vent impedances. (ii) Time constants were obtained from the flow step response data in (i) and plotted versus vent impedance to show that response time increases (i.e., τ increases) as impedance increases. (iii) Maximum attainable pressure increases as impedance increases. Average values and standard deviations are plotted for three trials per vent impedance in which three different dispensing tips were used as separate vent impedance samples. (iv) Fluidic and (v) equivalent electrical models of the gate and source–drain along with the sensors used in the experimental setup for data collection.

Referring to the results in Figure 5, a trade-off exists between fast time constants and the maximum pressure the amplifier can modulate to drive a load. We observe a linear relationship for both curves in Figure 5Aii,Bii. Each linear fit has an R^2 value of at least 0.98. An asymptote equal to the input pressure applied to the source–drain is shown as a dotted line and represents the case where the vent is blocked.

Given the analysis on flow dynamics described in Section S7, Supporting Information, we chose to incorporate a vent with an impedance of $0.74 \text{ kg mm}^{-4} \text{ s}^{-1}$ for both the source–drain and gate. The total response time of the system is estimated to be 1.39 s, which is the sum of the two individual time constants of 0.60 (gate) and 0.79 (source–drain) s.

5. Amplifier Characterization

We quantified the performance of the fluidic amplifier in terms of the metrics listed previously—gain and response time. A

schematic of the final amplifier design and its associated electrical analog are shown in Figure 6A,B. The amplifier in Figure 2A has a final mass of 46 g, height of 30 mm, and diameter of 44 mm. Note that the size has not been optimized and can be scaled down significantly by reduction in the input cavity gate volume and length of the gate tip.

Unlike the tests used to inform the final design, in the following characterization experiments we coupled the gate with the source–drain by constraining them in a 3D printed enclosure with an acrylic disc that helped fix the components in place. We separated the gate and source–drain so that the indenter tip rested just above the membrane in its default position. An amplifier body was omitted from the full amplifier device in the following experiments to enable full visualization, making quantitative and qualitative assessments of the active amplifier possible. In addition, the vent sizes used were selected based on the design selection process discussed previously. For the following experiments, Figure 6A,C shows the placement of the sensor hardware used to collect the measurements plotted in Figure 6B,D,E.

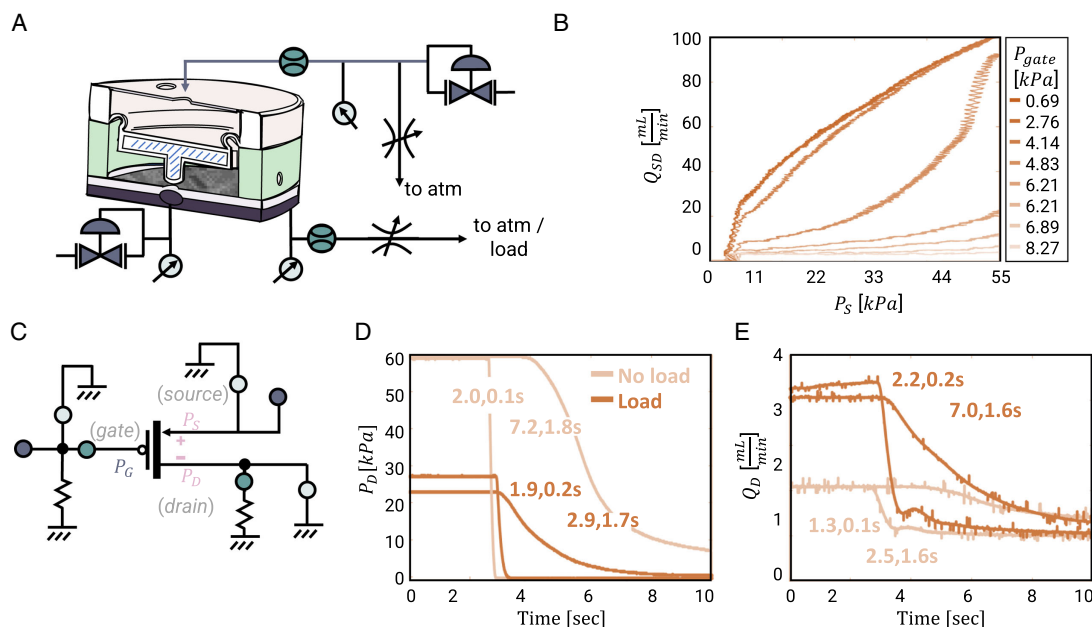


Figure 6. Final amplifier design characterization. A) Fluidic schematic of the amplifier and associated experimental hardware connections. B) I - V curve equivalent of an electrical pMOS transistor where flow through the source-drain channel is measured for increasing pressure at the source. The family of curves represents various gate input pressures ranging from 0.69 to 8.3 kPa. C) Analogous electrical diagram of the fluidic amplifier represented as a pMOS class-A amplifier and associated experimental hardware. D) Step response of the drain output pressure for various loading and gate input conditions. Dark purple lines correspond to amplifiers whose step response was measured in the presence of a load while blue correspond to amplifiers whose step response was measured in the presence of a no load. Two values are paired to each curve detailing gain and response time in seconds. Comparing curves within the same loading condition reveals the trade-off between gain and response time. E) Step response of the source-drain output flow.

5.1. Amplifier Gain

We collected flow-pressure characteristic curves to map out the amplifier's behavior. Similar to I - V curves for transistor characterization, these curves give us insight into the amplifier's operation by mapping the relationship between the output flow rate and the applied input pressure. The fluidic I - V curves are the resulting flow rate measurements at the drain from sweeping through source-drain pressures ranging from 0 to 55 kPa. Each curve represents a gate pressure input (IN_1) between 0.6 and 8.3 kPa.

Given an actuator and its associated pressure requirements for full actuation, a designer can use Figure 6C to identify the minimum required control pressure (i.e., IN_1) necessary to operate the amplifier. The pressure required by the actuator is denoted here as IN_2 . The rightmost portion of each curve that represents pressures larger than IN_2 can be further inspected to select an input pressure that also satisfies actuator flow input requirements. Flow requirements determine actuation speed for the desired task of the robot. The achievable output flow from the source-drain increases with increasing IN_1 . Therefore, a designer can analyze the tradeoff between lowering the gain of the system by selecting a larger IN_1 with a larger output flow to drive an actuator. A designer may need to take into consideration the maximum pressure available from the microfluidic circuit supplying the input control signal that acts as IN_1 .

In addition, if it is possible to vary the pressure of the microfluidic control signal, then IN_1 has the ability to vary and ultimately modulate the source-drain flow (Q_{SD}) while IN_2 remains constant. This means that by modulating the pressure at the gate, we can achieve a continuous amplification where the output is proportional to the input.

5.2. Amplifier Response Time

The latency of the fluidic circuits that we envision is the sum of the response times of each component in the circuit which includes logic, power, and analog operations. According to McDonald et al.'s^[12] review of typical operating speeds, pressure-driven soft fluidic actuators have response times on the order of seconds or longer; some exceptions such as Mosadegh et al.'s^[8] high-speed robot operating at 20 Hz were noted. With this in mind, our aim was to not impede the overall system response time by designing for an amplifier with a larger bandwidth than a microfluidic circuit and soft actuator at the input and output of the amplifier, respectively. The current design presented in this article has a minimum response time of 1.39 s according to the results in Figure 5 which is within the same order of magnitude as typical soft fluidic actuators. The response time increases at the cost of a lower gain which is a similar trade-off described by an electronic amplifier's gain-bandwidth product. The trade-off is evident in Figure 6D,

E. When comparing two curves, those with higher gains will have lower response time. We also note that loading the amplifier reduces its gain. Load has no significant impact on response time—this is most likely a consequence of the in-house pressures used as the supply to the inputs which are accompanied by very large flow rates. For future work, we provide insights to minimize the response time of the amplifier by performing design optimization, and we further discuss possible directions for future design improvement in the discussion section.

The experimental setup is detailed schematically in a fluidic and electrical sense in Figure 6A,B, respectively. A detailed description of the experimental setup and data collection is provided in Section S8, Supporting Information. The flow data were fitted to an analytical model (see Section S13, Supporting Information) of the electrical circuit equivalent of the full amplifier system: two cascaded RC circuits shown in the electrical analogue associated with the derivation of the aforementioned equation (see Section S12, Supporting Information). The final system response includes a linear summation of two exponential terms, each with different time constants expressed as a nonlinear function of resistance and capacitance of the gate and source–drain. The equation shows us the system's sensitivity to the resistances and capacitances associated with the gate, source–drain, and vents. We are able to tune the response times by tuning materials and geometries of the design to modify the associated resistances and capacitances.

5.3. Robustness

We tested the robustness of the fluidic amplifier by applying a cyclic 34.5 kPa step input at 0.5 Hz while a constant flow ran through the source–drain under examination at 103.4 kPa. Four samples were tested.

The minimum number of cycles that all the samples were able to withstand amounted to three hundred. One out of the four samples was able to reach 1000 cycles without showing changes in output pressure or flow. Those which failed at an intermediate number of cycles experience consistent failure at the membrane–indenter interface. The primary source of failure is the membrane at the closure site. We tested the full amplifier with inputs simulating the largest stresses it could experience which occurs when the gate input is at the maximum we expect from a microfluidic device at 34.5 kPa and the source–drain is at the maximum we expect from a soft actuator at 103.4 kPa. One sample reduced in pressure and flow rate consistently over the tests, suggesting that it was leaky from the start; however, the amplifier was able to drive a load throughout the entirety of the test.

We hypothesize that the difference in material modulus between the source–drain membrane and gate tip is the main cause of the failure. A tear is typically observed around the site where the tip meets the membrane. During closure of the source–drain, the gate tip pushes down into the channel which is simultaneously ballooning out around the tip due to the high pressures inside the channel causing regions of large extension and stress. Future studies can optimize that interface. We recommend performing material optimization studies to mitigate the stresses concentrating at this site and to insert an intermediate

material to avoid a step change in material modulus between the gate tip and membrane.

The gate, on the other hand, was able to undergo thousands of cycles without failure.

6. Demonstration

We demonstrated the capabilities of the fluidic amplifier in Figure 7 by comparing the ability of a fluidic circuit to drive a single-chamber, bending soft actuator made of SmoothSil-950 (Smooth-On Inc.)^[32] with and without our fluidic amplifier. An electromechanical pressure regulator (ITV1011) was used to emulate a microfluidic signal of 10.3 kPa and 50 mL min^{−1}. The source was pressurized at 38.1 kPa for a gain of 3.7.

The resultant actuation trajectories are shown in Figure 7Bi,Ci. Without the amplified signal, the maximum actuator bend angle is 20.5°. Supplying the actuator an amplified signal allows the actuator to bend fully to 50.9°. Electrical diagrams of the setup for this demonstration are provided, see Figure 7Bii,Cii.

An additional demonstration is provided in Movie S1, Supporting Information. The video shows the resultant bending angle of an actuator when driven with and without an amplifier for a constant pressure input. In addition, the actuator is actuated with a periodic input at 0.2 Hz. The pressures occurring simultaneously at the source–drain and gate provide insight to the varying gain as a result of the sinusoidal input. The volumetric flow rate data at the drain show the ability of the amplifier to reduce flow into the actuator (i.e., close the source–drain). Positive flows correspond to flows going into the actuator and negative flows are those in the direction from actuator to the vent during closure of the source–drain.

7. Discussion and Conclusions

In this article, we present the design, fabrication, and characterization of a soft fluidic power amplifier. We introduced four potential frameworks for a high gain valve design: microfluidic channel scaling, fluid entrainment, mechanical instabilities, and mechanical advantage.

While the approach based on microfluidic channel scaling can increase flow rates dramatically (i.e., due to the R^{-4} scaling of the fluidic impedance), larger features in an elastomeric device may suffer from insufficient structural support and collapse. An alternate approach to increasing flow rates is to use copies of a given circuit in parallel. By making many copies of the same microfluidic circuit, a larger flow output can be obtained without jeopardizing the circuit's structural integrity as suggested by Hoang et al.^[33] Both enlarging the channels and making multiple copies of a circuit increase output flow of the system. However, for applications emphasizing miniaturization, these two approaches inherently add volume (and complexity for the case of parallel circuits).

Although fluidic entrainment has potential for controllable flow amplification (as is evidenced by the large number of works published in the second-half of the 20th century^[34–36]), the field agrees that the wall attachment methods are a bit of a “black-art.”^[37] However, multiple publications have investigated the

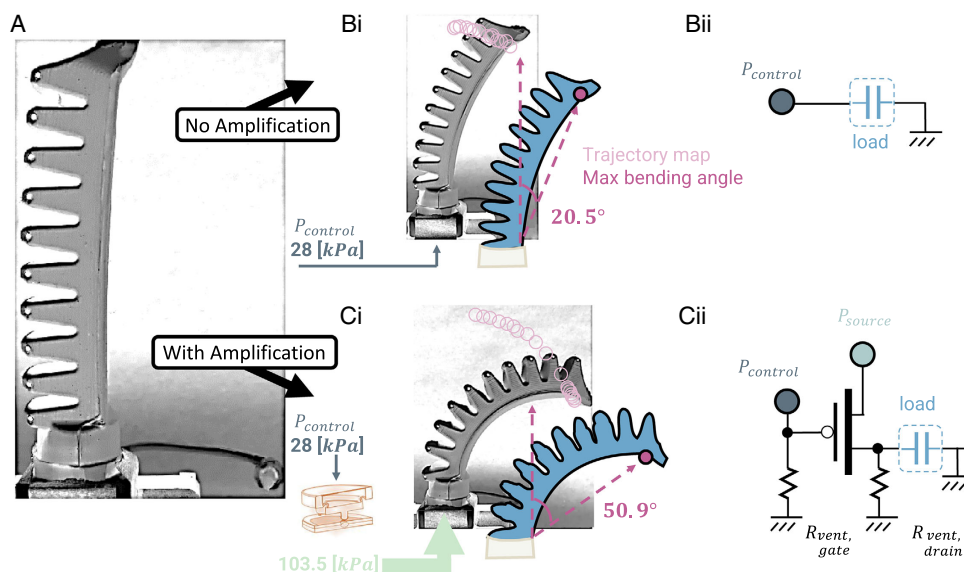


Figure 7. Comparison of driving a soft actuator with and without the fluidic amplifier. A) Image of the single-chamber pneumatic actuator with no control input. Bi) Image of single-chamber pneumatic actuator driven directly by a microfluidic control input signal. Ci) Image of single-chamber pneumatic actuator driven by a simulated microfluidic control input signal amplified by the fluidic amplifier. (Bi,Ci) A schematic of the fluid paths into the actuator are provided. A trajectory map is overlaid on an image of the actuator in light pink, demonstrating the full path taken by the tip of the actuator at constant time intervals during actuation. Lastly, the image and graphic are snapshots of the actuator at maximum deflection for each case which are noted in dark pink. Bii,Cii) An analogous electrical diagram describes the setup of the demonstrations. The diagrams both include a load, appropriate venting, and a simulated microfluidic control input signal. (Cii) includes the fluidic amplifier depicted as a class-A pMOS circuit architecture.

effects of the various design parameters.^[18,38] Although not a straightforward design challenge, the authors recommend further investigation of this design in cases where a low-impedance load is used.

We explored flow amplifier designs using this phenomena by studying a wall attachment prototype based on the work of Tesař.^[37] Prototypes of the device were constructed using a laminar fabrication technique similar to the pneumatic devices developed by Groenhuis et al.^[21] The device proved to work for low impedance loads but lost its ability to manipulate a high-flow stream in the presence of a load. We attribute the lack of functionality to the additional back pressure the load introduces which interferes with the pressure differential needed to conduct the wall attachment.^[39]

Circuits using components that leverage mechanical instabilities have successfully proven to control relevant flow rates and pressures for soft robotics. A bistable valve is able to achieve a gain of six for a state 0 to state 1 transition (see Figure 1); however, it requires higher pressures for a state 1 to state 0 transition, resulting in a lower gain of 1.36 when switching off. Although these circuits have successfully demonstrated flow control at relevant flow rates and pressures for soft robotics, the individual valves are rather large (approximately 10 mm³) and rely on non-scalable fabrication techniques. In addition, pressure and flow control using mechanical instabilities are inherently binary due to the strong nonlinearity in these mechanisms. We seek a more linear approach to allow for continuous actuator control.

Gain from mechanisms that leverage a pressure-controlled mechanical advantage has been explored in microfluidics and soft robotics. Weaver et al.^[19] created a multilayer valve

architecture with a rigid disk inclusion which acted as the key component for amplification. A low-pressure input acted on the full surface area of the disc while a higher pressure acted over a smaller area (i.e., the orifice area) which led to force amplification with a gain of 22 and the ability of the valve to close a channel. Song et al.^[20] produced CMOS amplifiers with a similar operating principle with gains up to 2.6. Instead of incorporating a disc, this work used a poppet structure to produce the surface area imbalance between the inlet and membrane diameters responsible for force amplification.

Our design is similar in principle to the works just mentioned. However, our amplifier takes advantage of nontraditional fabrication techniques for microfluidics in order to create the 3D geometries and material inclusions key to the overall performance. The main fabrication methods we used are injection molding and basic molding/casting. First, by using injection molding, we are able to create small, complex 3D features (e.g., features containing internal voids and undercuts) which are nearly impossible using a laminar fabrication approach such as soft lithography. Second, by avoiding plasma bonding, an integral step in soft lithography, we are not constrained to only using materials compatible with plasma bonding; rather, we can use materials with lower shore hardnesses which contribute to higher gains.

We demonstrated a fluidic amplifier capable of producing a pressure gain of approximately four at 0.2 Hz—sufficient for controlling soft robots from low pressure/flow microfluidic circuits. Higher gains can be achieved with further consideration of gate tip and source–drain channel cavity alignment and spacing; we believe this is the next critical step to maximize gain.

In this first iteration of the design, we defined key performance metrics (i.e., gain, output pressure, and bandwidth), explored various architectures, and characterized performance across a range of key geometric and material parameters. We conclude with a critical demonstration—operating a soft fluidic actuator with and without the amplifier in place, demonstrating both the limitations of driving soft actuators directly from microfluidic circuits, and the benefit of our proposed amplifier circuit.

Future investigations will focus on system optimization. The most obvious directions for improvement include minimizing the gate input cavity volume for a faster response time, a deeper exploration of membrane materials (which play a significant role in achievable gains), and a reduction in the size of the void cavity encapsulated by the amplifier body which can improve response times for a normally closed amplifier. In addition, the system was grounded by external means during the demonstration. Grounding is necessary for the amplifier gate tip to be able to effectively push down on the source–drain channel. Incorporating a strain limiting mesh or alternative means would free the amplifier from its dependence on rigid external ground connections.

Characterizing the performance of a normally closed amplifier would allow us to develop new amplifier architectures inspired by electronic analogues—for example, class-B or class-AB amplifiers—to meet different performance goals. A normally closed amplifier can be constructed from the same components that we presented in this article; the only requirement is a translation of the gate input to the body in which case the input port would access the cavity which lies between the bottom face of the gate head and the top face of the source–drain.

Lastly, the integration of snap-through instabilities for a volume-controlled (rather than absolute pressure-controlled) amplifier has the potential to dramatically increase the response time and efficiency of the system, albeit with a more binary response. The work presented here is a step toward highly complex soft robots that make use of fluidic elastomer-based microcontroller equivalents for autonomy.

8. Experimental Section

Fabrication: All parts associated with the source–drain were cast in 3D printed molds printed by Polyjet printers (Object Scholar and Connex) using Vero Blue material (Stratasys). All parts associated with the gate were printed using Vero Clear (Stratasys). Injection molding techniques were used^[40] to create the molds used to fabricate the gate. Traditional molding techniques are not capable of producing the internal shapes and undercuts necessary to create the 3D features of the gate. In addition, alternatives to classic molding techniques as listed in ref. [41] were also not suitable to create thin features such as the hinge of the gate.

Insert cores were printed on an FDM printer in a carbon fiber reinforced nylon material (Onyx, Markforged, MA, USA). STL files for all molds used in this project are available (see S1 Data File S1). We used the elastomers Ecoflex 0030 (Smooth-On Inc., PA, USA), Ecoflex 0010 (Smooth-On Inc., PA, USA), True Skin 30 (CHT USA–Richmond, VA, USA), and Smooth-Sil 945 (Smooth-On Inc., PA, USA) as the primary valve materials. The Supporting Information contains step-by-step descriptions of how to prepare the elastomer solutions, how to assemble the molds, the casting process, and how to construct the amplifier and add necessary vents, tubing, and connections to power sources. Fabrication processes, material selection, and assembly are detailed in Section S6, S10, and S11, Supporting Information.

Testing Methods: We tested and validated out design concepts using custom test setups, a mechanical testing machine, and FEA. First, we used Abaqus (SIMULIA, Providence, RI), a finite element software, to conduct finite element studies to inform the design of the gate. We validated the FEA results and conducted experiments on the source–drain channel to inform its design using a mechanical testing machine (Instron 5567, Instron, MA, USA). Custom 3D printed (Onyx) fixtures were used to complete these tests. A pressure regulator (ITV1011) and waveform generator (Rigol DG5072) were used for a subset of tests to control pressure inputs while three-way toggle switches and manual gauges regulated the in-house air supply for all experiments. Data were collected using three independent 0–15 psi (0–103.4 kPa) gas board-mount analog pressure sensors (ABP Series, Honeywell International Inc., TX, USA) and a 5 mL min^{−1} volumetric flow rate meter (Model 50 Series Gas Mass Flow Meter, McMillan, TX, USA). Data were recorded by a NI-DAQ USB-6008 (National Instruments Corp., TX, USA) and the data were processed on a PC using MATLAB. The components used during testing were cyclically loaded until their stress–strain relationships no longer changed significantly at the maximum pressures and forces that they would be subject to during the experiments. The Supporting Information contains detailed descriptions of each experiment.^[42]

Supporting Information

Supporting Information is available from the Wiley Online Library or from the author.

Acknowledgements

This work was supported by grants from the Office of Naval Research (award #N00014-17-1-2063) and the National Science Foundation (award #DMR-1420570). Any opinions, findings, and conclusions or recommendations expressed in this material are those of the authors and do not necessarily reflect the views of the National Science Foundation.

Conflict of Interest

The authors declare no conflict of interest.

Data Availability Statement

The data that support the findings of this study are available from the corresponding author upon reasonable request.

Keywords

fluidic amplifiers, fluidic logic, microfluidics, soft controllers, soft robotics

Received: May 10, 2022

Revised: June 24, 2022

Published online: September 22, 2022

- [1] S. Abundance, C. B. Teeple, R. J. Wood, *IEEE Rob. Autom. Lett.* **2020**, 5, 55025509.
- [2] C. Oneill, T. Proietti, K. Nuckols, M. E. Clarke, C. J. Hohimer, A. Cloutier, D. J. Lin, C. J. Walsh, *IEEE Rob. Autom. Lett.* **2020**, 5, 38993906.
- [3] E. W. Hawkes, L. H. Blumenschein, J. D. Greer, A. M. Okamura, *Sci. Rob.* **2017**, 2, 8.

- [4] X. Huang, K. Kumar, M. K. Jawed, A. M. Nasab, Z. Ye, W. Shan, C. Majidi, *Sci. Rob.* **2018**, 3, eaau7557.
- [5] N. R. Sinatra, C. B. Teeple, D. M. Vogt, K. K. Parker, D. F. Gruber, R. J. Wood, *Sci. Rob.* **2019**, 4, 33.
- [6] S. Li, D. M. Vogt, D. Rus, R. J. Wood, *Proc. Natl. Acad. Sci.* **2017**, 114, 1313213137.
- [7] M. A. Robertson, O. C. Kara, J. Paik, *Int. J. Rob. Res.* **2021**, 40, 72.
- [8] B. Mosadegh, A. D. Mazzeo, R. F. Shepherd, S. A. Morin, U. Gupta, I. Z. Sani, D. Lai, S. Takayama, G. M. Whitesides, *Lab Chip* **2014**, 14, 189.
- [9] J. Yin, R. Hinchet, H. Shea, C. Majidi, *Adv. Funct. Mater.* **2021**, 31, 2007428.
- [10] B. Jumet, M. D. Bell, V. Sanchez, D. J. Preston, *Adv. Intell. Syst.* **2021**, 2100163.
- [11] M. Wehner, R. L. Truby, D. J. Fitzgerald, B. Mosadegh, G. M. Whitesides, J. A. Lewis, R. J. Wood, *Nature* **2016**, 536, 451.
- [12] K. McDonald, T. Ranzani, *Front. Rob. AI* **2021**, 131, 266.
- [13] N. W. Bartlett, K. P. Becker, R. J. Wood, *Soft Matter* **2020**, 16, 5871.
- [14] R. Z. Gao, C. L. Ren, *Biomicrofluidics* **2021**, 15, 011302.
- [15] C. Majidi, *Adv. Mater. Technol.* **2019**, 4, 1800477.
- [16] E. G. Hevia, L. De La Rochefoucauld, R. J. Wood, in *Int. Conf. on Robotics and Automation (ICRA)*, IEEE, Piscataway, NJ **2022**, pp. 7138–7144.
- [17] K. W. Oh, K. Lee, B. Ahn, E. P. Furlani, *Lab Chip* **2012**, 12, 515.
- [18] J. W. Joyce, *Fluidics: Basic Components and Applications*, U.S. Army Electronics Research and Development Command, Harry Diamond Laboratories, 2800 Powder Mill Road, Adelphi, MD 20783 **1983**.
- [19] J. A. Weaver, J. Melin, D. Stark, S. R. Quake, M. A. Horowitz, *Nat. Phys.* **2010**, 6, 218.
- [20] S. Song, S. Joshi, J. Paik, *Adv. Sci.* **2021**, 8, 2100924.
- [21] V. Groenhuis, S. Stramigioli, *IEEE/ASME Trans. Mechatron.* **2015**, 21, 1604.
- [22] D. J. Preston, P. Rothmund, H. J. Jiang, M. P. Nemitz, J. Rawson, Z. Suo, G. M. Whitesides, *Proceedings of the National Academy of Sciences* **2019**, 116, 7750.
- [23] S. Xu, Y. Chen, P. H. Nak-seung, K. P. Becker, R. J. Wood, *Proc. Natl. Acad. Sci.* A dynamic electrically driven soft valve for control of soft hydraulic actuators, **2021**, 118, e2103198118.
- [24] M. Wehner, M. T. Tolley, Y. Menguc, Y. Park, A. Mozeika, Y. Ding, C. Onal, R. F. Shepherd, G. M. Whitesides, R. J. Wood, *Soft Robot.* **2014**, 4, 263.
- [25] R. F. Shepherd, F. Ilievski, W. Choi, S. A. Morin, A. A. Stokes, A. D. Mazzeo, X. Chen, M. Wang, G. M. Whitesides, *Proc. Natl. Acad. Sci.* **2011**, 108, 20400.
- [26] M. T. Tolley, R. F. Shepherd, B. Mosadegh, K. C. Galloway, M. Wehner, M. Karpelson, R. J. Wood, G. M. Whitesides, *Soft Rob.* **2014**, 1, 213.
- [27] N. S. Usevitch, Z. M. Hammond, M. Schwager, A. M. Okamura, E. W. Hawkes, S. Follmer, *Sci. Rob.* **2020**, 5, 40.
- [28] N. D. Naclerio, A. Karsai, M. Murray-Cooper, Y. Ozkan-Aydin, E. Aydin, D. I. Goldman, E. W. Hawkes, *Sci. Rob.* **2021**, 6, 55.
- [29] F. Shen, M. Ai, J. Ma, Z. Li, S. Xue, *Micromachines* **2020**, 11, 914.
- [30] P. N. Duncan, T. V. Nguyen, E. E. Hui, *Proc. Natl. Acad. Sci.* **2013**, 110, 18104.
- [31] N. Pamme, *Lab Chip* **2007**, 7, 1644.
- [32] C. B. Teeple, T. N. Koutros, M. A. Graule, R. J. Wood, *Int. J. Robot. Res.* **2020**, 39, 1647.
- [33] S. Hoang, K. Karydis, P. Brisk, W. H. Grover, *PLoS One* **2021**, 16, e0254524.
- [34] G. S. Aneja, **1972**.
- [35] C. Mangion, R. Salvinski, N70-39042, **1970**.
- [36] T. M. Weathers, *J. Spacecr. Rockets* **1973**, 10, 417.
- [37] V. Tesar, in *EPJ Web of Conf.*, Vol. 25, EDP Sciences, Proceedings of the National Academy of Sciences 500 Fifth Street NW NAS 339 Washington, DC 20001 **2012**, p. 01093.
- [38] M. Cycon Jr, D. Schaffer, *Design Guide for Laminar Flow Fluidic Amplifiers and Sensors, Technical Report*, Garrett Pneumatic Systems Div, Phoenix, AZ **1982**.
- [39] D. Bain, <https://www.springer.com/us/book/9783211811481> (accessed: October 1970).
- [40] M. A. Bell, K. P. Becker, R. J. Wood, *Adv. Mater. Technol.* **2021**, 7, 2100605.
- [41] F. Schmitt, O. Piccin, L. Barbe, B. Bayle, *Front. Robot. AI* **2018**, 5, 84.
- [42] A. N. Gent, *Rubber Chem. Technol.* **1996**, 69, 59.

Supplementary Information: High-gain microfluidic amplifiers: The bridge between microfluidic controllers and fluidic soft actuators

Elizabeth Gallardo Hevia Connor M. McCann Michael Bell Nak-seung Patrick Hyun Carmel Majidi
Katia Bertoldi Robert J. Wood**

Elizabeth Gallardo Hevia

Harvard University, Cambridge, USA

gallardo@g.harvard.edu

Connor McCann

Harvard University, Cambridge, USA

cmccann@g.harvard.edu

Dr. Michael Bell

Harvard University, Cambridge, USA

bell@seas.harvard.edu

Dr. Patrick Hyun

Harvard University, Cambridge, USA

nphyun@g.harvard.edu

Prof. Carmel Majidi

Carnegie Mellon University, Pittsburgh, USA

majidi@andrew.cmu.edu

Prof. Katia Bertoldi

Harvard University, Cambridge, USA

katia.bertoldi78@gmail.com

Prof. Robert J. Wood

Harvard University, Cambridge, USA

rjwood@seas.harvard.edu

1 Rigid insert used in Gate design

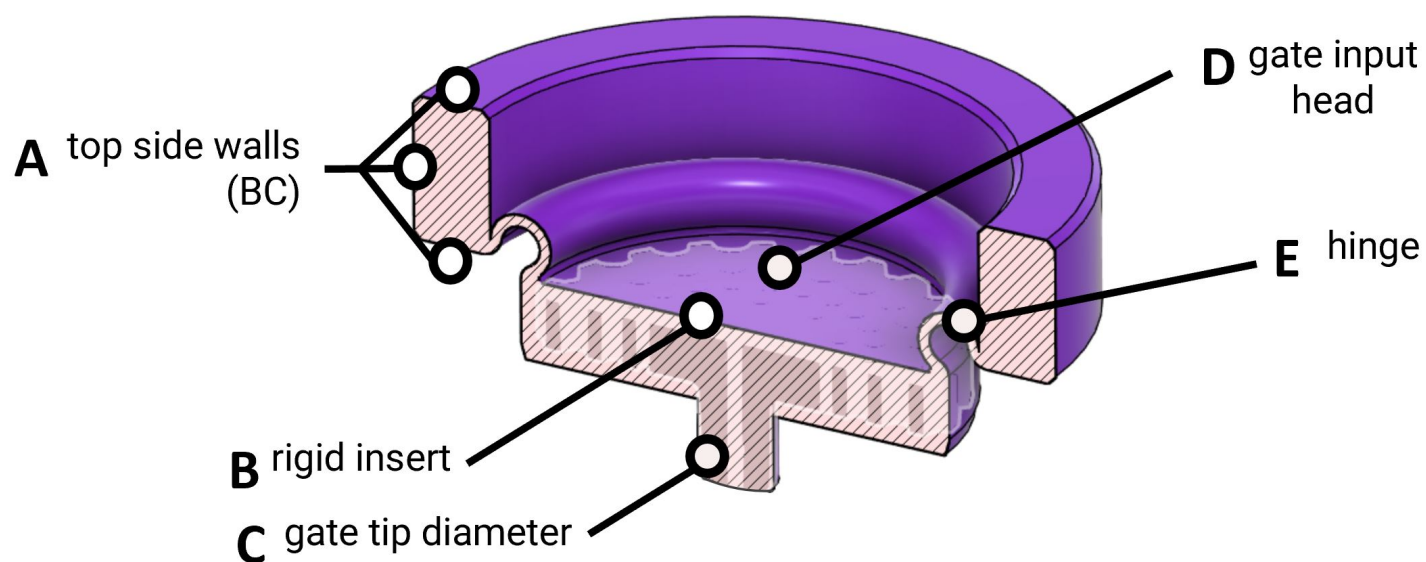


Figure S1: Cross sectional view of a 3D CAD rendering by Fusion360 of the gate. (A) The top side walls that are designated a fixed boundary condition for FE simulations are identified. (B) The location where the rigid insert lies within the gate is highlighted. (C) The gate tip diameter is labelled for reference. (D) The gate input head is labelled for reference. (E) The hinge is a critical component of the gate and a focus of the FE simulations.

2 Finite element model setup

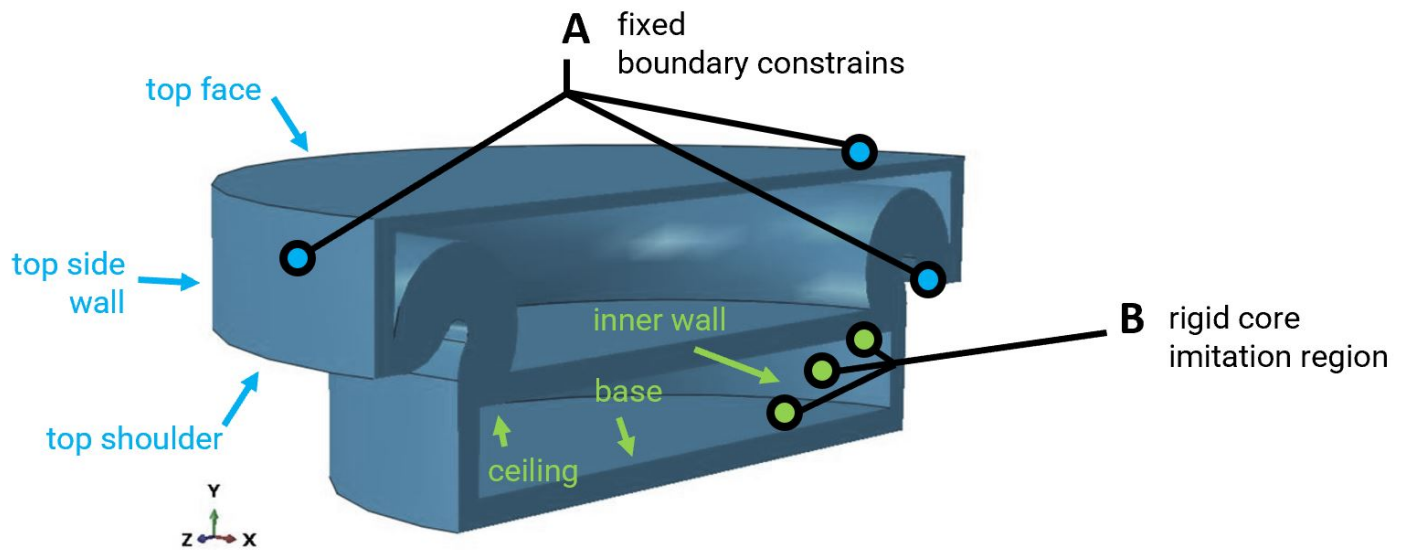


Figure S2: Cross section view of a 3D CAD rendering by Abaqus of one of the various gate designs used in the parameter study. The model shown is for a gate with a 2.5 mm thick hinge, 14 mm head diameter, and hinge eccentricity equal to 0 (i.e., circular hinge). (A) Fixed boundary constraints were applied to the top face, top side walls, and top shoulder (labelled in blue) of the gate are fixed in space. (B) A predefined displacement is assigned to the region where a rigid core would be inserted which is made up of a cavity with a ceiling, base, and inner wall (labelled in green).

We leveraged finite element (FE) simulations using the commercial finite element software Abaqus (SIMULIA, RI, USA) to better understand how gate parameters affect the performance of the fluidic amplifier. We created geometric models using the 3D modelling CAD software Fusion360 (Autodesk, CA, USA). We imported the geometry using .IGES files into Abaqus. The material of the gate, True Skin 30 (CHT-Silicones, VA, USA), was modeled using an incompressible Gent constitutive model¹ (via a UHYPER user-defined subroutine) with a shear modulus of $G = 0.16$ [MPa] and an extension limit of $J_m = 10^6$, as identified from uniaxial tensile testing. The gate was meshed using 8-node hybrid, linear isoparametric brick elements (C3D8H). A mesh size of 0.75 mm was used, with a finer 0.35 mm mesh size at the hinge where higher strains were observed.

We conducted static simulations studies, to simulate the force produced throughout a range of gate tip extensions for relevant input pressures. The top covering, top side walls, and top shoulder faces (see Figure S2 for gate component locations) were fixed in space (see SI Section S2). A ramping input pressure was slowly applied to the gate cavity. Once the gate cavity was pressurized, the gate tip was displaced 4 [mm] (or until self contact occurred) to mimic the distance the tip would need to travel for full valve closure. Recall, a rigid insert is used in the gate to maximize force transfer to the gate tip. To simplify the model, we avoided using a rigid part in our model instead we created a void where the rigid insert would normally live and assumed this portion of the gate would not deform. The displacement boundary condition was applied to the inner walls of the void (see SI Section S1 and S2).

The accuracy of our numerical analyses were experimentally verified (see Figure S2) and will be discussed further in the next section; therefore, we used our simulations to investigate the effect of the parameters on force-displacement curves. The force-displacement curves are indicators of the achievable gain for each gate design variation. Particularly, we simulated the response of 27 gate designs with different values of the hinge thickness (1.0, 1.5, 2.5 [mm]), hinge eccentricity (linear, elliptical, circular), and gate input head diameter (10, 12, 14 [mm]).

3 Gate FEA validation experiments: experimental setup and FEA model validation

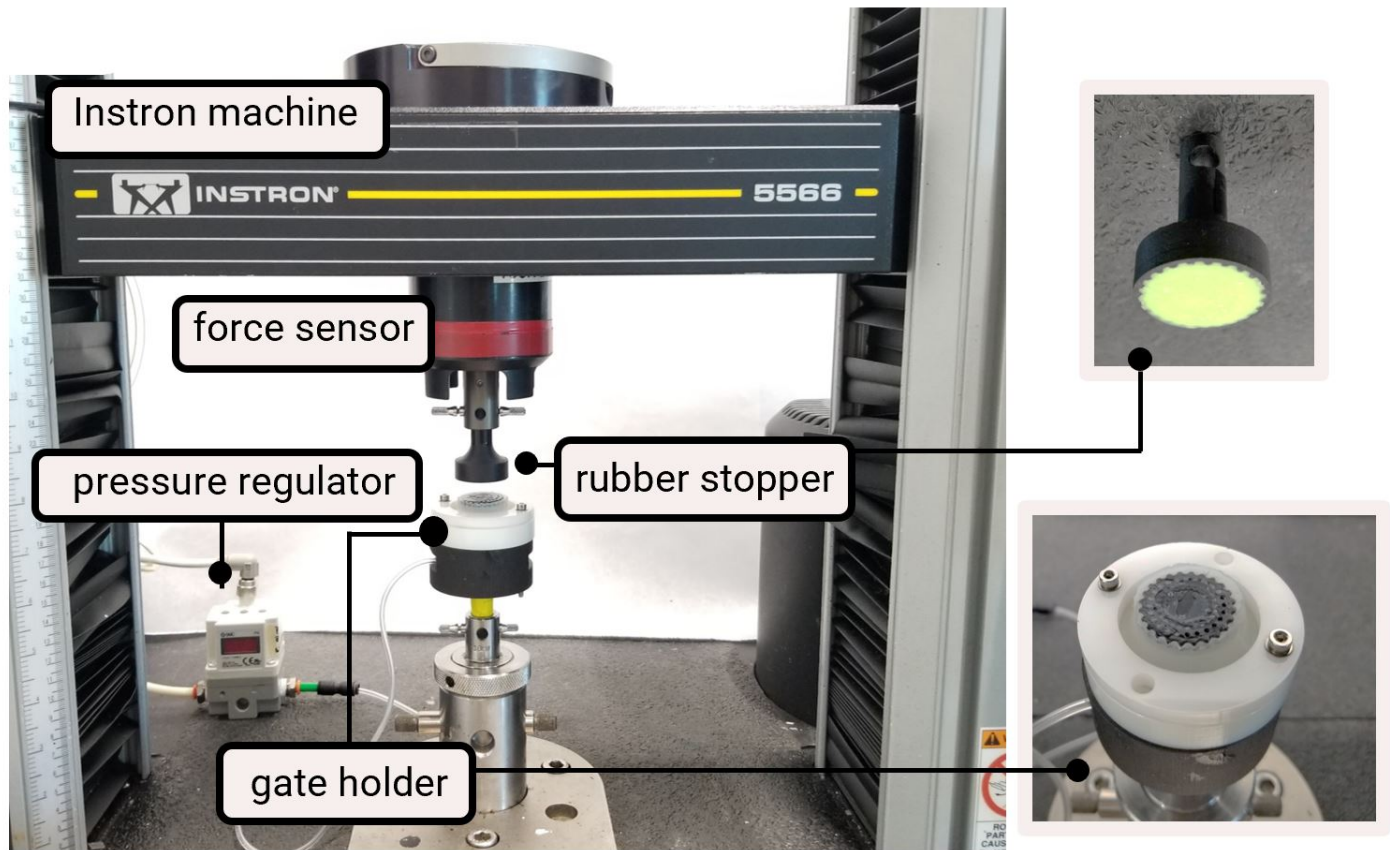


Figure S3: Image of the experimental setup used to collect force-displacement measurements to validate finite element simulations. The equipment used in this test are labelled. A larger image of the rubber stopper and gate holder are provided for visual clarity. The gate is placed in the gate holder and clamped down by an acrylic disk, nuts, and bolts. After the gate is inflated, the Instron machine collects force measurements while pushing down into the inflated gate. The pressure regulator set the gate pressure to the relevant pressure magnitudes and maintains the pressure while the rubber stopper pushes down into the gate input head.

To validate our finite element simulations, we compared force-displacement behaviour obtained from the simulation results with those obtained by fabricated devices tested on a mechanical testing machine (Instron 5567, Instron, MA, USA) with a 100 [N] load cell. In order to fix the gate in place, a custom rig was 3D printed to hold the gate in place which we labelled as *gate holder* in Fig. S3. A second custom fixture held a flat stamp-like piece whose bottom base was covered with silicone (Double Elite 32, Zhermack, NJ, USA) labelled as a Fig. *rubber stopper* in S3. We removed the tip of the gate design to simplify this test. We note that the force produced by the indenter core is equivalent for any tip diameter. To complete the validation tests, pressures ranging from 7 to 35 kPa were applied to the gate with a pressure regulator (ITV1011). We then measured the force produced by the gate for a displacement range of 0 to 3.5 [mm] after pressurizing the gate to the various pressure inputs. Once the gate was inflated, the rubber stopper was set to displace downwards pushing the gate down to its original configuration. The initial position of the *gate input head* without a pressure input was measured. We used this value to dictate when to stop the rubber stopper from pushing down and start moving back up which we considered as one cycle. Three cycles were taken for each sample, with three different samples for each design. The averaged results and standard deviations of the three samples are plotted along with FEA results for selected gate designs in Fig. S4.

We tested six representative devices; each was chosen to hold two of the three parameters constant as

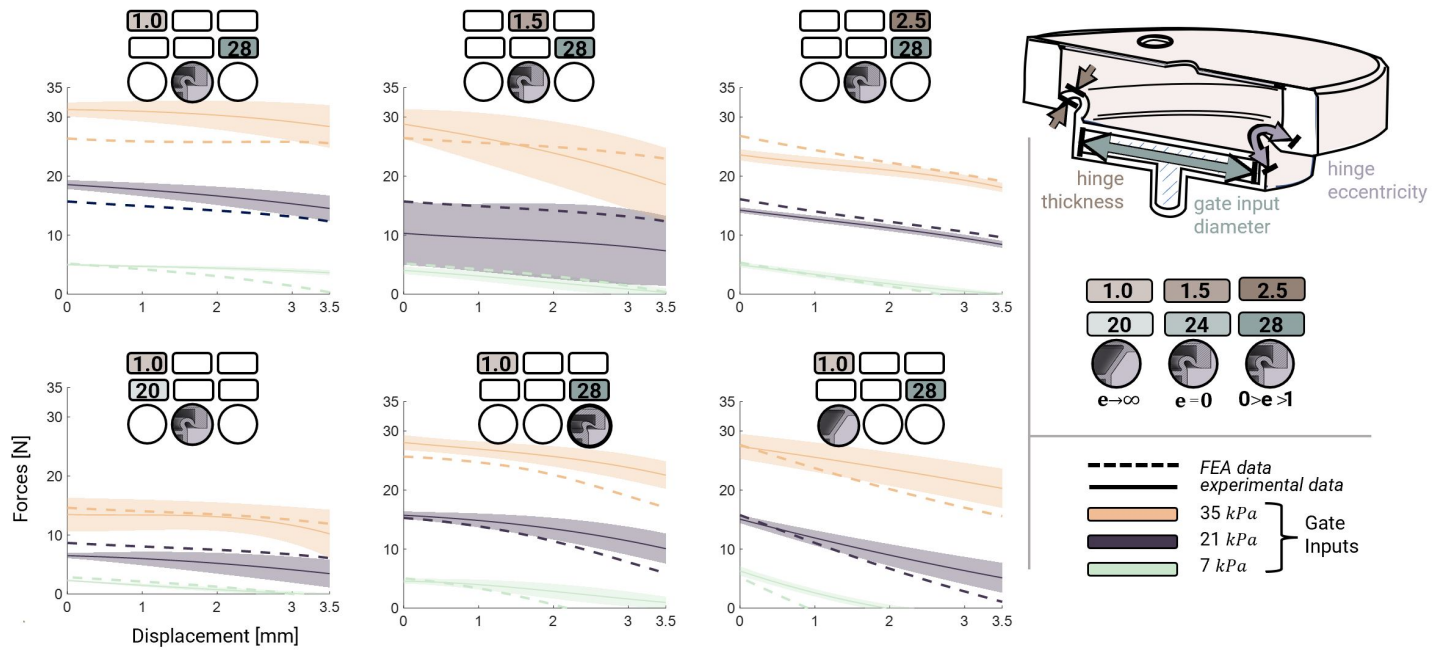


Figure S4: Force-displacement plots displaying simulated and empirical data for six different gate designs. Curves in each plot correspond to varying gate pressure inputs indicated by color. Data obtained from FE simulations are shown in dashed lines while the corresponding empirical data is shown in solid lines with standard deviation clouds made from three trials per samples – three samples were tested per design. The various gate design parameters for each design are specified by the filled-in boxes above each plot. The parameters corresponding to each box are specified in the key; the parameters include hinge thickness, gate input diameter, and hinge eccentricity.

controls while changing one of the parameters. In this way, we could compare at least two devices to acquire an understanding of the trend for that particular parameter. In this test we also included the final gate design which has a hinge thickness of 1.5 [mm], a gate input diameter of 14 [mm], and an eccentricity of zero.

In order to rely on the simulation results to better understand the effect of the different parameters on the ability to produce high gains, we verified that the numerical simulations were reflecting the trends seen by our devices. Indeed, the trends were captured as seen in Fig. S4.

4 Definition of gate hinge eccentricity and dead-zone

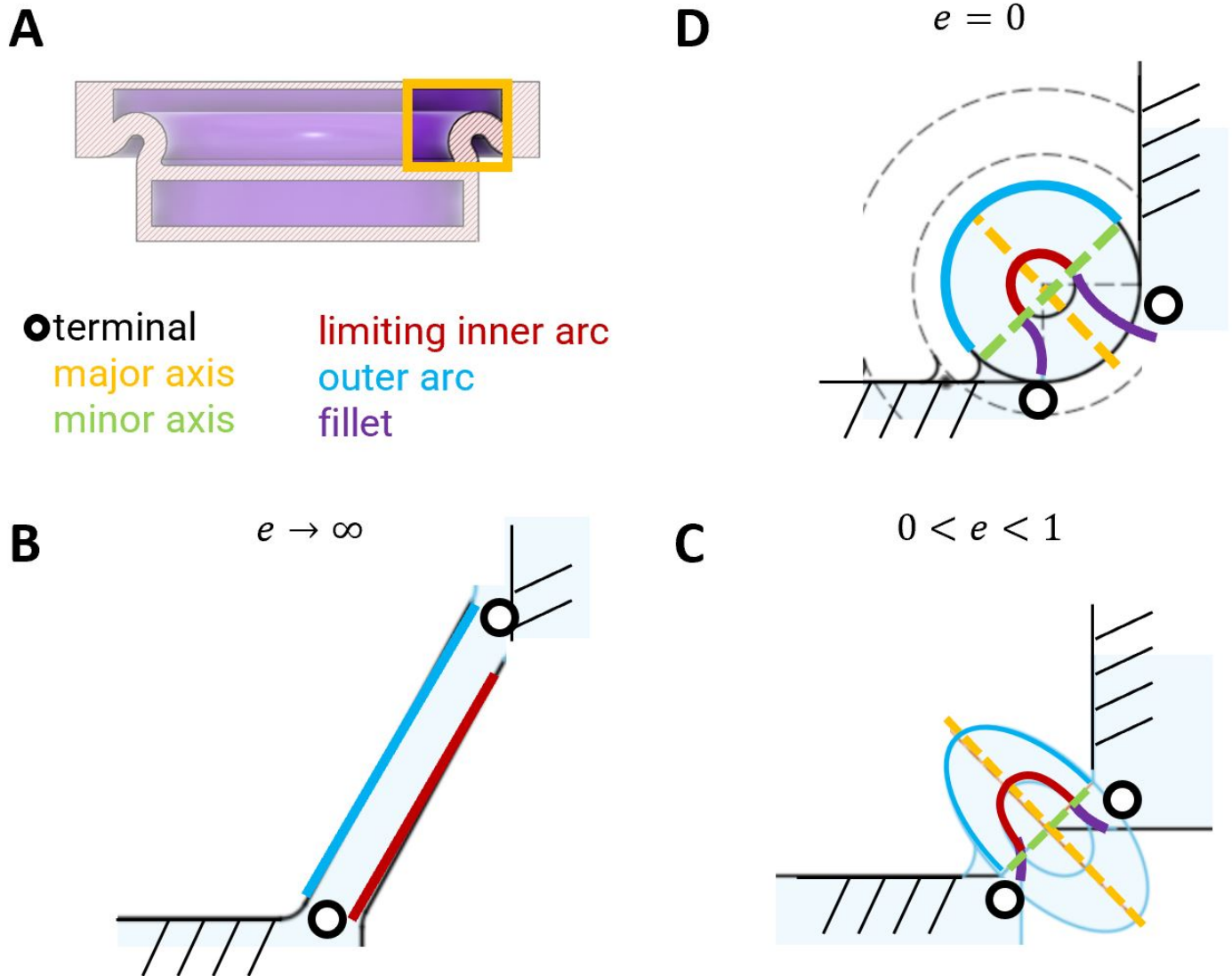


Figure S5: (A) A cross sectional view of a 3D CAD rendering of a gate with a circular hinge. The area containing the hinge is boxed in orange. 2D sketches of the boxed area for gates containing different hinge eccentricity types are provided in B-D. Key parameters of the hinges are identified and color-coded. (B) A 2D sketch of a linear hinge. (C) A 2D sketch of an elliptical hinge. (D) A 2D sketch of a circular hinge (the major and minor axes are equal in length). The minor axes of both elliptical and circular hinges are equal in length. Due to the larger major axis in the elliptical hinge, the length of the limiting inner arc of the elliptical hinge is longer than that of the circular hinge.

Eccentricity, e , is a measure of the similarity of a conic section to a circular shape. We define the eccentricity of the various hinge designs by treating them as portions of conic shapes. To define eccentricity we use the ratio between major and minor axes of the hinges indicated in orange and green in Fig. S5. The figure zooms into the hinge to further describe the parameters that we use to define eccentricity. Eccentricity approaching infinity defines a linear curve. Therefore, the linear hinge is assigned an eccentricity approaching infinity, see Fig. S5-B. An intermediate curved hinge was assigned an eccentricity between 0 and 1 which by definition describes an ellipse, see Fig. S5-C. In this case, the major and minor axes are not equal – this is true for both the inner and outer arc. We assign an eccentricity of 0 to the circular hinge, see Fig. S5-D. By definition, an eccentricity of zero defines a circle. In this case, the major and minor axes are equal for both the inner and outer arcs.

For both the circular and elliptical hinges, the minor axes of the inner arc are 0.5 [mm]; only the minor axis of the outer arcs are displayed. However, the fillet that connects the inner arc to the rest of the gate

are not equal in length. These lengths contribute to the “deadzone” of the hinge. The deadzone will be defined for the purpose of this paper as the range of hinge extension in which the gate can travel vertically downward while experiencing minimal resistive forces from the hinge. The deadzone is the slack in the hinge which is the difference between the distance the hinge has to move and the length of the inner path in the hinge. The distance the hinge has to move is the distance between the connections points of the terminals of the hinge. The total inner path attributed to the hinge is the sum of the limiting inner arc and the fillets connecting the inner arc to the terminal.

We note that a flexure with eccentricity approaching infinity acts like a spring being stretched axially with a linear force-displacement relationship (force-displacement relationships are shown in Figure 3). The resistive forces of the hinge are initiated the moment the gate receives an input pressure and can be denoted by a large negative slope. However, this is not observed for hinges containing eccentricities of 0 to 1 because of their deadzones. The deadzone allows the gate to move downward without imparting resistive forces from the hinge. This translates to a minimal loss in force in the FD curves throughout the range of extensions shown.

5 Source-drain design space study – experimental setup

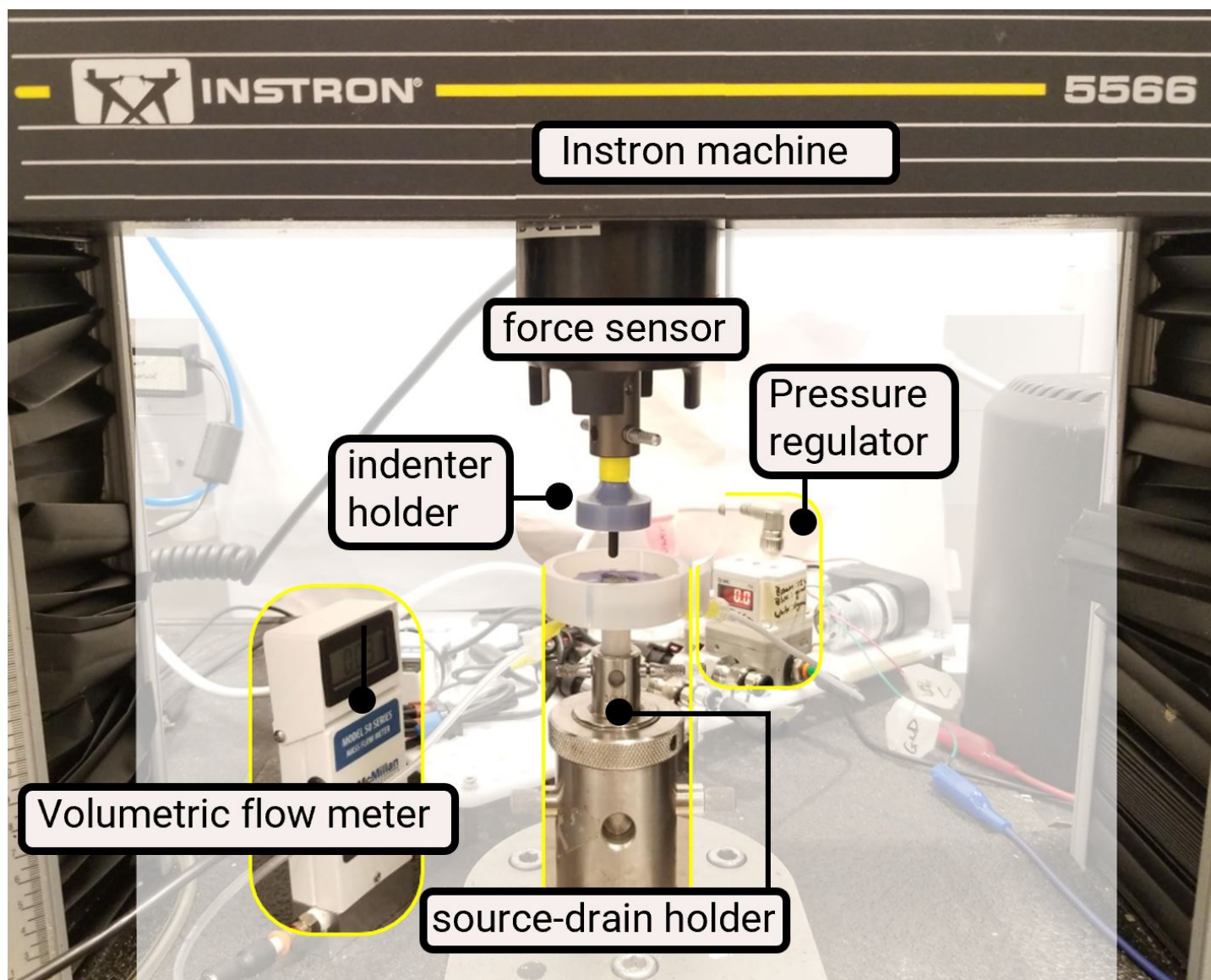


Figure S6: Image of the experimental setup used to collect force-displacement measurements used to evaluate the design space associated with the source-drain channel. The equipment used in the tests are labelled.

Data for the force-displacement plots collected was obtained by fixing the source-drain elastomer structure on a mechanical testing machine (Instron 5567, Instron, MA, USA) with a 100 [N] force sensor. In parallel, we collected volumetric flow rate measurements with a 5 [L/min] volumetric flow meter (McMillan, TX, USA). The flow meter and mechanical testing machine were not synchronized. However, maximum force for closure, a flow profile, the duration of the source-drain on-to-off switching event, and maximum flows were captured. Data was collected for three trials for three different samples of each source-drain design.

The set up of the experiment is shown in Figure S6. The source-drain under testing was secured in a source-drain holder while a rigid core with tip diameter measuring 9.5 [mm] was coupled to the force sensor by a custom indenter holder.

For each test, the source-drain was pressurized to 34.5, 68.9, and 103.5 [kPa] while its output was connected to a volumetric flow meter. The core was set initially at the zero marker and then moved downwards at a rate of 0.25 [mm/sec] into the source drain until less than 0.2 [$\text{mL} \cdot \text{min}^{-1}$] was observed on the flow meter's digital screen. The Zero extension marker corresponds to the top of the source-drain component when the source-drain is deflated. A non-zero force value was observed at the zero marker

at the start of a test after inflating the source-drain with the appropriate pressure input.

6 Source-drain channel fabrication and assembly

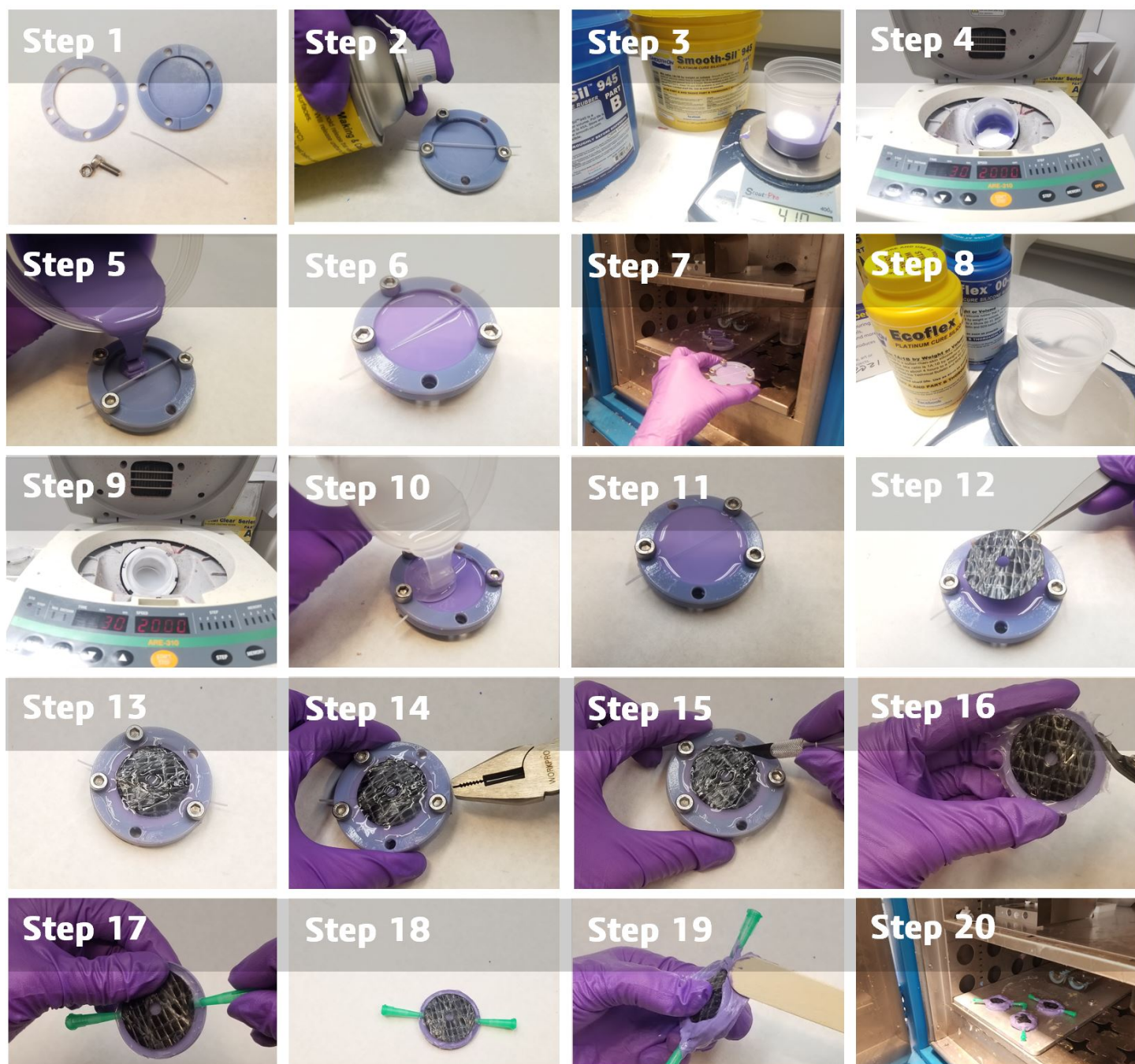


Figure S7: The amplifier's source-drain channel is made using fabrication approaches familiar to the field of soft robotics including traditional molding and casting methods.

The source-drain channel is fabricated using the following steps:

1. Collect parts that make up the mold: mold base, plate, rod, nuts, and bolts. The flow layer molds were 3D-printed on an Objet30 Scholar 3D printer (Stratasys Ltd.) using VeroBlue (RDG840) material. After printing, the molds were mechanically cleaned of support material and baked at 90°C for at least 24 hours.
2. Before molding, spray Ease Release 200 (Mann Formulated Products, Macungie, PA, USA) or an equivalent release agent on all surfaces of the mold. This will facilitate removal of the elastomer once it is cured.

3. Pour the appropriate weight ratio of the elastomer of your choosing. All the materials used in this design, including EcoFlex 0010, EcoFlex 0030, and Smooth-Sil 945, were mixed at a 1:1 weight ratio.
4. Mix the elastomer using a planetary mixing machine (Thinky, CA, USA).
5. Pour mixed elastomer into the mold to create the base of the channel that will create the source-drain.
6. Pour up to the halfway point of the rod, leaving the top half of the rod uncovered by elastomer.
7. Place elastomer into a 65°C oven for 3 minutes. This will cure the SmoothSil-945 just enough so that the elastomer poured on top will not mix with the base elastomer; the elastomer will also remain sufficiently uncured to create a strong bond between the two layers.
8. Mix elastomer for the appropriate membrane material. In this project we used EcoFlex 0010 and EcoFlex 0030 both which were mixed at a 1:1 weight ratio.
9. Mix the elastomer using a planetary mixing machine.
10. Pour membrane elastomer.
11. Fill up the rest of the mold until the elastomer reaches the rim of the mold. Two variations for the top plate were used in this project. Each was designed with a different thickness to conduct tests to compare designs containing membranes of different thicknesses.
12. Place a circular piece of inextensible fabric (ripstop coated sailcloth, Dimension Polyant, DE) at the center of the mold, noting that too much pressure can cause the elastomer to pour out. In addition, motion of the fabric around could trap bubbles under the fabric. A bubble at the near the center hole can be detrimental to performance.
13. The piece of fabric should be centered over the rod. The center hole should be an access point to the channel within the source-drain component. Place the mold back in the oven at 65°C for 10 minutes or until fully cured.
14. Remove the rod using pliers.
15. Use an exacto knife or tweezers to release the elastomer from the walls and remove it from the mold.
16. Trim the cast device of any flashing. Flashing can be prevented by improved clamping to avoid gaps between the base and plate mold.
17. Insert tubing connection ports (dispensing Tips with Luer Lock Connection, McMaster Carr, IL, USA) into the terminals of the channel.
18. Ensure that the connection ports are aligned with the channel.
19. Secure the connection ports with uncured SmoothSil-945.
20. Place in the oven. Repeat the previous step until there are no leaks and the connection ports are robust. Add more support material around the fabric edges if necessary to avoid ballooning of the membrane.

7 Experimental setup to characterize the effect of vent impedances on gate and source-drain performance

Studies were performed to determine step responses, time constants associated with each step response, and the maximum attainable pressures for the gate and source-drain designs containing varying vent impedances as shown in Figure 5. Each test was performed for the gate and source-drain separately. Plastic dispensing tips of gauges 18 to 25 (i.e., 1.2 to 0.5 [mm]) orifice diameters (Dispensing Tips with Luer Lock Connection, McMaster Carr, IL, USA) were used as venting nozzles. Using an Ohm's law equivalent ($V = IR \rightarrow P = QR$)² we calculated impedance values of 0.082 to 0.74 [$\frac{kg}{mm^4.s}$].

Time constants were determined using the step responses observed in each system. A 20 [kPa] step input pressure was applied at the gate and 55 [kPa] at the source-drain using a manual toggle switch and pressure regulator (ITV1011, SMC Corporation of America, IN, USA). Flow and electrical diagram equivalents of the experimental setups are shown in Figure Figure 5-Aiv,Biv and Av,Bv, respectively, where pressures and flow rates were measured at the locations indicated. The flow rate through the vent resistors were estimated using first-order low-pass dynamics as is discussed in SI Section S11. Empirical data was fit to Equation 3 and the time constant, τ , was extracted from the fitted model.

We chose a final vent size with an impedance of 0.74 [$\frac{kg}{mm^4.s}$] for both the source-drain and gate based on the trends observed in Figure 5-A. The total response time of the system is estimated to be 1.39 [s] (the sum of the two individual time constants of 0.60 (gate) and 0.79 (source-drain) [s]). Due to these impedances, the maximum pressure from the gate is expected to be attenuated by 3% of the original input source signal while at the source-drain the output pressure experiences a drop of 17%. The pressure loss is not unexpected as a pressure drop always accompanies fluid flow through a channel due to the friction between the fluid and channel walls. Therefore, the estimated gain shows that it preserves 86% of the ideal gain; further details on the derivation of the estimated gain are described in the Supplementary Information Section S15.

8 Experimental setup and data collection methods for system gain and response time tests

The full system responses for the electrical equivalent of the amplifier shown in Figure 6 are derived in this section. The final fluidic amplifier, including a combined gate, source-drain channel, and vents, was characterized. The experimental setup includes a gate input (IN_1), source-drain input (IN_2), appropriate vents for the gate and source-drain ($R_{V,G}$, $R_{V,SD}$), pressure sensors, and flow rate meters.

The test setup used to collect the data in Figure 6-B consists of the hardware labeled in Figure 6-A,C. We used a volumetric flow sensor capable of measuring flows ranging from 0-5 [mL·min⁻¹] (Model 50 Series Gas Mass Flow Meter, McMillan, TX, USA) and three pneumatic pressure sensors capable of measuring pressures from 0-103.5 [kPa] (ABP Series, Honeywell International Inc., TX, USA). We measured the input pressure as well as the pressure after the source-drain resistor and the flow in series with the vent. Lastly, we measured pressure at the input of the source to obtain (IN_2).

We collected flow-pressure characteristic curves to map out the amplifier's behavior. Similar to I-V curves for transistor characterization, these curves give us insight into the amplifier operation by mapping the relationship between the output flow rate and the applied input pressure. We increased the source-drain pressure from 0 to 55 [kPa] while collecting flow rate measurements at the drain. We repeated the task for various gate pressure inputs (IN_1) ranging from 0.69 to 8.3 [kPa].

The test setup used to collect the data in Figure 6-D,E consists of the hardware labeled in Figure 6-A,C.

An input pressure was applied by an in-house supply while regulated by a custom setup manual regulators and analog pressure readers. At time 0 [s] a toggle switch was used to open a valve to the gate input to simulate a step-down response at the drain. Pressure measurements were taken at the drain preceding the load and at the gate. Flow measurements were taken at the source-drain and gate. We performed the experiment for 3 different gate and source-drain combinations. We adjusted the pressure inputs at the gate and source to demonstrate the trade-off between gain and response time.

9 Gate fabrication and assembly



Figure S8: The amplifier's gate is made using fabrication approaches familiar to the field of soft robotics including injection-molding with elastomers.³

The following steps are used to fabricate the gate:

1. Collect all parts that make up the mold. Molds were 3D printed using an Objet30 inkjet-based 3D printer (Stratasys, Eden Prairie, MN, USA) from VeroClear (RGD810) material. A clear mold helps verify that the elastomer is flowing through the mold during injection.
2. Before molding, spray Ease Release 200 (Mann Formulated Products, Macungie, PA, USA) or an equivalent release agent on all surfaces of the mold.
3. Begin assembling the mold by aligning the pieces that form the hinge of the gate above the top piece.

4. Place rigid core at the center of the mold.
5. Insert necessary nuts, bolts, and washers.
6. Close off the mold with the final bottom piece.
7. Clamp the mold tightly. The mold must be clamped properly to ensure that the elastomer flows throughout the mold during injection.
8. Back view of the assembled mold.
9. Front view of the assembled mold.
10. Before injecting silicone into the molds, the two unmixed elastomer components were loaded into a Nordson EFD 1500 mL cartridge (Nordson EFD, East Providence, RI, USA), degassed, and the cartridge plungers were inserted, see Bell et al.³ for further details. The elastomer was purged until no striations were observed to ensure proper mixing.
11. The elastomer was then dispensed at 685 kPa (100 PSI) into the injection port of the mold.
12. The material was injected until it overflowed from the mold vents and air bubbles were no longer observed. This process took approximately 1 minute to complete.
13. Place the mold in a 65°C oven for 30 minutes or until the overflow material is fully cured.
14. Remove the cured material on the mold to access the screw heads.
15. Remove the screws.
16. Remove the bottom mold cover.
17. Image of the disassembled mold and cured gate component laying in the top mold.
18. Remove gate component using tweezers.
19. Remove parts of the cast device that were created as a result of the venting ports.
20. Image of various gate pieces in different orientations.

10 Fluidic amplifier assembly and setup

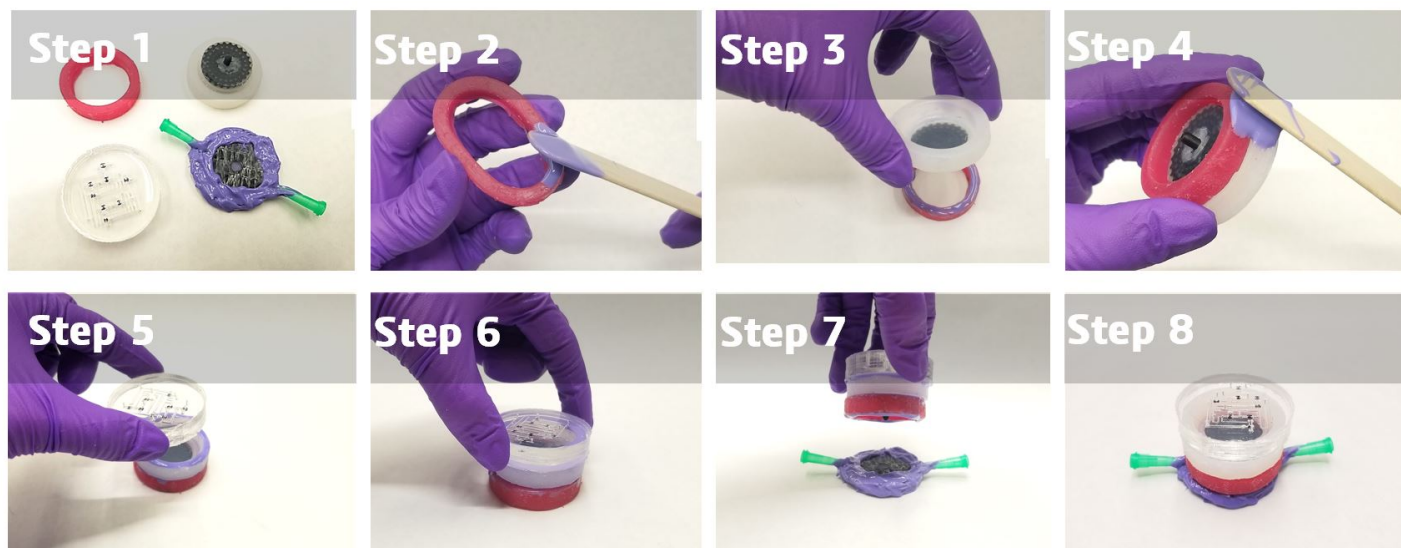


Figure S9: The fluidic power amplifier assembly consists of wet bonding the various subcomponents which include a lid, the gate, a support body, and the source-drain channel.

The following steps were used to assemble the complete amplifier:

1. Assemble all the components that make up the amplifier: a lid, the gate, a support body, and the source-drain channel.
2. Apply uncured SmoothSil-945 onto a face of the support body.
3. Stack the gate and support body. Tap lightly to ensure that the two faces are in contact. Place in a 65°C oven for 5 minutes for a partial cure. This will facilitate handling of the device while bonding the remaining components.
4. Apply SmoothSil-945 to any gap between the body and gate as necessary. This step secures the structure of the amplifier. However, a complete seal is not required. In fact, gaps between the two parts are encouraged to allow the device to vent when actuated.
5. Apply uncured SmoothSil-945 onto the face of the gate and place the lid on top. Place assembly in a 65°C oven for 5 minutes. In the image, an elastomer piece with an embedded microfluidic circuit is used as a lid to demonstrate the integration potential of these two components. The lid must contain an input port to drive the amplifier.
6. Tap on the lid lightly to ensure that the lid and gate faces are in contact. It is important to create a seal between these two components. Venting is only desired when controlled by the designed venting ports.
7. Apply uncured SmoothSil-945 onto the source-drain and place the currently assembled amplifier onto the source-drain. Place assembly in a 65°C oven for 5 minutes.
8. Image of the fully-assembled fluidic power amplifier.

11 Derivation of analytical model for vent tests

The analytical model used to describe the inclusion of vents to the gate and source-drain is derived in this section. These equations are used to understand how vent impedance effects gate and source-drain response times, gain, and maximum attainable output pressures.

To derive impedance values for the dispensing tips used in the the tests described in SI Section S7, we use Ohm's Law on the basis of the electrical analogy commonly used in microfluidics² to estimate the fluidic resistance associated with the dispensing tip. In the analogy, voltage (V), current (I), and electrical resistance (R) are analogous to pressure (P), flow rate (Q), and fluidic resistance (R_f), respectively. To calculate resistance, a known pressure was applied to the input of a tube connected in series to the dispensing tip and the corresponding flow rate was measured.

$$V = IR \sim P = QR_f \quad (\text{S.1})$$

Electrical circuit analogs of the experimental setup used to calculate system gain and response time are shown in Figure 5-Aiii,Biii. The flow rate through the vent resistors is estimated using first-order low-pass dynamics as shown in Equation (3).

The time constants, $\tau = R_{total}C_{total}$, plotted in Figure 5-Ai,Bi for each step response were obtained by fitting the volumetric flow rate data through the vent to Equation (3). The response time can be tuned by varying the following parameters. For the source-drain,

$$R_{total} = \frac{R_{SD}}{R_{V,SD}}(R_{SD} + R_{V,SD})$$

$$C_{total} = C_L$$

whereas at the gate,

$$R_{total} = \frac{R_{V,G}}{R_G}(R_{V,G} + R_G)$$

$$C_{total} = C_G$$

12 Derivation of fluidic amplifier response time (full system)

The flow data was fitted to an analytical model, see Equation (S.2), of the electrical circuit equivalent of the full amplifier system, see Figure S10: two cascaded RC circuits shown in the electrical analogue associated with the derivation of the aforementioned equation. The final system response includes a linear summation of two exponential terms each with different time constants expressed as a nonlinear function of resistance and capacitance of the gate and source-drain. To obtain the coefficients, we used the time responses derived earlier from Figure 5: 1.5 [s] (gate vent) and 0.92 [s] (source-drain vent).

$$V_{CG,SD} = A_{G,SD}e^{-\lambda_1 t} - B_{G,SD}e^{-\lambda_2 t} + V_{GSD} \quad (\text{S.2})$$

where,

$$\lambda_1, \lambda_2 = \frac{-[\omega_1 \cdot (1 + \alpha_1) + \omega_2(1 + \alpha_2)] \pm \sqrt{[\omega_1 \cdot (1 + \alpha_1) - \omega_2(1 + \alpha_2)]^2 + 4\omega_1 \cdot \omega_2 \cdot \alpha_1 \cdot \alpha_2}}{2}$$

and,

$$\begin{aligned} \omega_1 &= \frac{1}{R_2 C_3} \\ \omega_2 &= \frac{1}{R_3 C_6} \\ \alpha_1 &= \frac{R_2}{R_1 + R_4} \\ \alpha_2 &= \frac{R_3}{R_1 + R_4} \end{aligned}$$

The total response time of the system is a sum of the two independent systems (i.e., gate and source-drain). The equation shows us the system's sensitivity to the resistances and capacitances associated with the gate, source-drain, and vents. We are able to tune the response times by tuning materials and geometries of the design to modify the associated resistances and capacitances.

13 Derivation of an analytical model for the full system response

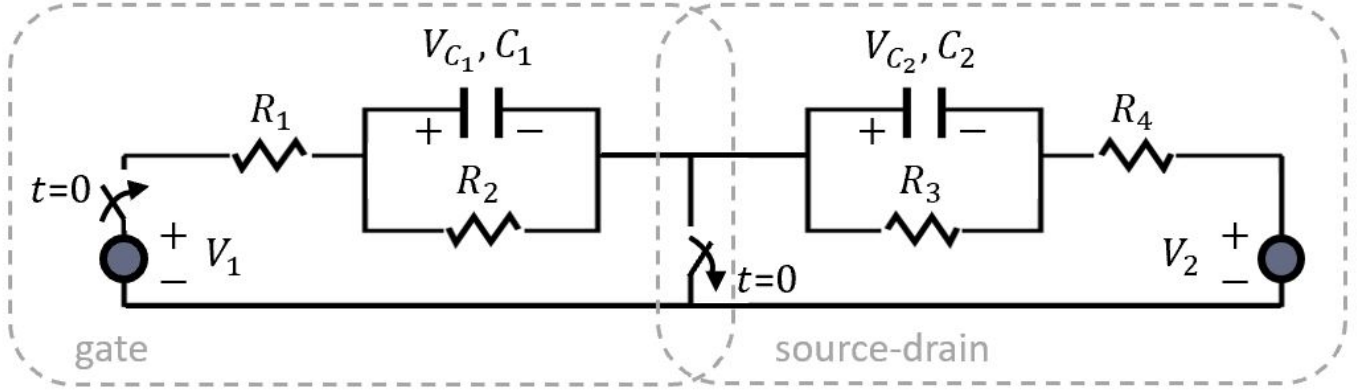


Figure S10: An electrical diagram of the full amplifier system made of a gate, source-drain, and vents. The gate and source-drain are separate entities which are boxed in a grey dashed line. The two entities interact with each other to produce a combined response. At time $t = 0$, the gate is given a command input pressure and consequently begins acting on the source-drain, which was fully pressurized before $t = 0$.

The full system responses for the electrical equivalent of the amplifier shown in Figure 6 are derived in this section. The gate circuit and the source-drain circuit are integrated in Figure S10, where R_1, R_2 and C_1 represent the gate vent resistance ($R_{V,G}$), the gate resistance (R_G), and the gate capacitance (C_G) for the gate circuit, respectively, and R_3, R_4 , and C_2 represent the source-drain vent resistance ($R_{V,SD}$), the source-drain resistance (R_{SD}), and the channel material capacitance (C_{SD}) for the source-drain circuit, respectively. The supplied input pressure to the gate (IN_G) is defined as an input voltage source, V_1 , and the supplied input pressure at the source-drain (IN_{SD}) is defined as an input voltage source, V_2 , in Figure S10.

The gate circuit is initially at rest such that the gate capacitor C_1 is initially fully discharged, and the source-drain circuit is initially fully charged at $t < 0$. Therefore the initial gate voltage and the source-drain voltage are given as

$$V_{C1}(0) := 0, V_{C2}(0) := \frac{R_3}{R_3 + R_4} V_2 \quad (\text{S.3})$$

At $t = 0$, the switching occurs and the charge within two capacitors will change accordingly as depicted in Figure S10.

The system equation for the gate voltage V_{C1} and the source-drain voltage V_{C2} are derived using Kirchhoffs Current Law and Kirchhoffs Voltage Law,

$$\frac{V_{C1}}{R_2} + C_1 \frac{dV_{C1}}{dt} - \frac{V_{C2}}{R_3} - C_2 \frac{dV_{C2}}{dt} = 0 \quad (\text{S.4})$$

$$V_1 - R_1 \left(\frac{V_{C1}}{R_2} + C_1 \frac{dV_{C1}}{dt} \right) - V_{C1} - V_{C2} - R_4 \left(\frac{V_{C2}}{R_3} + C_2 \frac{dV_{C2}}{dt} \right) - V_2 = 0. \quad (\text{S.5})$$

Now, suppose that $x = [V_{C1}; V_{C2}] \in \mathbb{R}^2$, the system equation can be simplified to a linear differential equation

$$M\dot{x} = Ax + B = Ax + bv \quad (\text{S.6})$$

where

$$M := \begin{bmatrix} C_1 & -C_2 \\ -R_1 C_1 & -R_4 C_2 \end{bmatrix}, A := \begin{bmatrix} -\frac{1}{R_2} & \frac{1}{R_3} \\ \frac{R_1}{R_2} + 1 & \frac{R_4}{R_3} + 1 \end{bmatrix}, b = \begin{bmatrix} 0 \\ 1 \end{bmatrix}, v = -V_1 + V_2.$$

Observe that the constant matrix M is invertible since $R_4, R_1, C_1, C_2 > 0$, where the determinant of M is

$$\det(M) = -R_4 C_1 C_2 - R_1 C_1 C_2 < 0,$$

and the inverse of M is

$$M^{-1} = \frac{1}{\det(M)} \cdot \begin{bmatrix} -R_4 C_2 & C_2 \\ R_1 C_1 & C_1 \end{bmatrix} = \frac{-1}{R_1 + R_4} \begin{bmatrix} -R_4 \frac{1}{C_1} & \frac{1}{C_1} \\ -R_1 \frac{1}{C_2} & \frac{1}{C_2} \end{bmatrix}.$$

We define ω_1 as the inverse of the time constant for an independent RC circuit with R_2, C_1 , and ω_2 as the inverse of the time constant for an independent RC circuit with R_3, C_2 :

$$\begin{aligned} \omega_1 &:= \frac{1}{R_2 C_1} \\ \omega_2 &:= \frac{1}{R_3 C_2}, \end{aligned}$$

and let the dimensionless positive parameters, $\alpha_1, \alpha_2 > 0$ be

$$\begin{aligned} \alpha_1 &:= \frac{R_2}{R_1 + R_4} \\ \alpha_2 &:= \frac{R_3}{R_1 + R_4}, \end{aligned}$$

then by multiplying M^{-1} to the left of Eqn (S.6) the system equation is simplified to a linear differential equation,

$$\dot{x} = \bar{A}x + \bar{b}v \quad (\text{S.7})$$

where

$$\bar{A} := \begin{bmatrix} -(1 + \alpha_1)\omega_1 & -\alpha_1\omega_1 \\ -\alpha_2\omega_2 & -(1 + \alpha_2)\omega_2 \end{bmatrix}, \bar{b} = \begin{bmatrix} -\alpha_1\omega_1 \\ -\alpha_2\omega_2 \end{bmatrix}.$$

Now, the characteristic equation for the system in Eqn (S.7) is computed as

$$\det(\lambda I - \bar{A}) = (\lambda + \omega_1(1 + \alpha_1))(\lambda + \omega_2(1 + \alpha_2) - \omega_1\omega_2\alpha_1\alpha_2) = \lambda^2 + \beta\lambda + \gamma = 0,$$

where, β, γ are positive since $\omega_1, \omega_2, \alpha_1, \alpha_2 > 0$,

$$\begin{aligned} \beta &= (\omega_1 + \omega_2) + \omega_1\alpha_1 + \omega_2\alpha_2 \\ \gamma &= \omega_1\omega_2(1 + \alpha_1 + \alpha_2). \end{aligned}$$

Therefore, the system is stable, and the corresponding eigen values are

$$\begin{aligned} \lambda_{1,2} &= \frac{-\beta \pm \sqrt{\beta^2 - 4\gamma}}{2} \\ &= \frac{-[\omega_1 \cdot (1 + \alpha_1) + \omega_2(1 + \alpha_2)] \pm \sqrt{[\omega_1 \cdot (1 + \alpha_1) - \omega_2(1 + \alpha_2)]^2 + 4\omega_1 \cdot \omega_2 \cdot \alpha_1 \cdot \alpha_2}}{2}, \end{aligned}$$

where λ_1 corresponds to $+$ and λ_2 corresponds to $-$ in the above equation. Since the $\alpha_1, \alpha_2, \omega_1, \omega_2$ are all positive, λ_1 and λ_2 are real and $\lambda_2 < \lambda_1 < 0$ holds. A state transformation to obtain a diagonal system using the similarity transformation matrix T composed of the eigenvectors of \bar{A} , denoted as $\nu_1, \nu_2 \in \mathbb{R}^2$ corresponding to the eigenvalues λ_1 and λ_2 , respectively. The transformation matrix is defined as

$$T = [\nu_1 \quad \nu_2] = \begin{bmatrix} 1 & 1 \\ b_1 & b_2 \end{bmatrix}$$

where

$$\begin{aligned} b_1 &= \frac{1}{\omega_1\alpha_1} \cdot (-\lambda_1 + \omega_1 \cdot (1 + \alpha_1)) \\ b_2 &= \frac{1}{\omega_1\alpha_1} \cdot (-\lambda_2 + \omega_1 \cdot (1 + \alpha_1)). \end{aligned}$$

Suppose that $\bar{x} = T^{-1}x$, then the transformed system equation can be written as

$$\dot{\bar{x}} = \begin{bmatrix} \lambda_1 & 0 \\ 0 & \lambda_2 \end{bmatrix} \bar{x} + \begin{bmatrix} d_1 \\ d_2 \end{bmatrix} v \quad (\text{S.8})$$

where

$$d_1 := \frac{\omega_1 \alpha_1 (-\alpha_1 b_2 \omega_1 + \alpha_2 \omega_2)}{\lambda_1 - \lambda_2}, d_2 := \frac{\omega_1 \alpha_1 (\alpha_1 b_1 \omega_1 - \alpha_2 \omega_2)}{\lambda_1 - \lambda_2},$$

which is well-defined since $\lambda_1 - \lambda_2 > 0$. The diagonalized system equation in Eqn (S.8) has an analytic solution for $\bar{x} := [\bar{x}_1; \bar{x}_2]$, assuming the input pressure v is constant,

$$\bar{x}_1 = e^{\lambda_1 t} \bar{x}_1(0) + \frac{d_1(e^{\lambda_1 t} - 1)}{\lambda_1} v \quad (\text{S.9})$$

$$\bar{x}_2 = e^{\lambda_2 t} \bar{x}_2(0) + \frac{d_2(e^{\lambda_2 t} - 1)}{\lambda_2} v \quad (\text{S.10})$$

where $\bar{x}_1(0) := [1 \ 0] T^{-1}x(0)$ and $\bar{x}_2(0) := [0 \ 1] T^{-1}x(0)$ and $x(0) = [V_{C1}(0); V_{C2}(0)]$ in Eqn (S.3). Finally, the response of the original state x can be obtained by $x = T\bar{x}$, and the general form of the response can be written as

$$V_{C1} = a_{C1}e^{\lambda_1 t} + b_{C1}e^{\lambda_2 t} + c_{C1} \quad (\text{S.11})$$

$$V_{C2} = a_{C2}e^{\lambda_1 t} + b_{C2}e^{\lambda_2 t} + c_{C2} \quad (\text{S.12})$$

for some constants $a_{C1}, a_{C2}, b_{C1}, b_{C2}, c_{C1}, c_{C2} \in R$.

14 Estimated system gain derivation.

We can estimate the gain of the amplifier that includes the impedances chosen described in SI Section S7 as follows:

$$Gain_{estimated} = \frac{P_{SD,estimated}}{P_{Gate,estimated}}$$

where,

$$\begin{aligned} P_{SD,estimated} &= P_{SD,ideal} \times (100 - 17\%) \\ P_{Gate,estimated} &= P_{Gate,ideal} \times (100 - 3\%). \end{aligned}$$

The reduction in the ideal pressure (i.e., deviation from the source pressure) is due to the additional impedances presented by the vents.

Ideal gain describes the maximum gain attainable given that no impedances exist in the system; ideal gain of the amplifier is based solely on the pressure input and output.

$$Gain_{ideal} = \frac{P_{SD,ideal}}{P_{Gate,ideal}}$$

By substituting the definition for ideal gain into the equation for estimated gain, the above equation can be rewritten as

$$\begin{aligned} Gain_{estimated} &= Gain_{ideal} \times \frac{1 - 0.17}{1 - 0.03} \\ Gain_{estimated} &= Gain_{ideal} \times \frac{0.83}{0.97} \end{aligned}$$

After simplification, the resultant estimated gain is a 86 % of the ideal.

$$Gain_{estimated} = Gain_{ideal} \times 0.86$$

References

- [1] A. N. Gent, *Rubber chemistry and technology* **1996**, *69*, 1 59.
- [2] K. W. Oh, et al., *Lab on a Chip* **2012**, *12*, 3 515.
- [3] M. A. Bell, K. P. Becker, R. J. Wood, *Advanced Materials Technologies* **2021**, 2100605.